Contents lists available at ScienceDirect

Chemical Geology

journal homepage: www.elsevier.com/locate/chemgeo

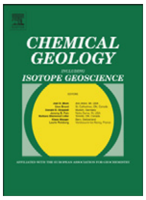

Single-shot laser ablation split stream (SS-LASS) petrochronology deciphers multiple, short-duration metamorphic events

Daniel R. Viete [a,b,*], Andrew R.C. Kylander-Clark [b], Bradley R. Hacker [b]

[a] *Department of Earth Sciences, Durham University, Durham DH1 3LE, UK*
[b] *Department of Earth Science, University of California Santa Barbara, Santa Barbara, CA 93106, USA*

A R T I C L E I N F O

Article history:
Received 23 January 2015
Received in revised form 14 September 2015
Accepted 16 September 2015
Available online 24 September 2015

Keywords:
U/Th-Pb geochronology
LA-ICP-MS petrochronology
Metamorphic time scales
Episodic metamorphism
Cordillera de la Costa
Venezuela

A B S T R A C T

Single-shot laser ablation split stream (SS-LASS) petrochronology offers spatial resolution of <1 μm per (surface) analysis. This enables the technique to interrogate metamorphic zircon overgrowths that are very thin, or that preserve a composite age structure. To demonstrate the advantages of SS-LASS, the technique was applied to metamorphic zircon overgrowths in five rocks from the Cordillera de la Costa, Venezuela. In these rocks, SS-LASS was able to decipher discrete, short-duration ($<10^6$ yr) zircon growth events at c. 33.0, c. 28.3, c. 23.0 and c. 18.2 Ma. Comparison with existing geo-/thermochronology suggests that the SS-LASS dates represent (hydro)-thermal events that mark distinct episodes of tectonism affecting the northern margin of South America.

With an external error of 5% incorporated into isotope ratios (as required to achieve satisfactory analytical precision), SS-LASS dates for reference materials were accurate to within 1.5% of published values. The SS-LASS technique is thus, in favorable cases, capable of providing $<10^6$ yr resolution for Cenozoic rocks. Methods in 'geospeedometry'—which employ forward models to reproduce observed diffusion length scales—have obtained anomalously short time scales of 10^4–10^6 yr for metamorphism. The high spatial and temporal resolution of SS-LASS offers tremendous promise for investigating the veracity of these claims.

1. Introduction

Some 'geospeedometry' studies using diffusion length scales to assess time scales for regional metamorphism have yielded surprisingly short estimates, in the range of 10^4–10^6 yr (Perchuk and Philippot, 1997; Camacho et al., 2005; Faryard and Chakraborty, 2005; Ague and Baxter, 2007; Raimbourg et al., 2007; Viete et al., 2011a; Spear et al., 2012; Spear, 2014). It has also been proposed that such short-duration regional metamorphism may be inherently non-uniform, comprising multiple 'episodes' of metamorphism on even shorter time scales of 10–10^5 yr (Camacho et al., 2005; Ague and Baxter, 2007, Viete et al., 2011b).

The diffusion parameters used for these estimates harbor significant uncertainty arising from extrapolation of laboratory diffusion data (generally obtained at T > 1000 °C) to temperatures of typical crustal metamorphism. They also consider only the time-integrated thermal response of the rock/minerals, and therefore provide limited information on the nature of non-uniformity in metamorphic processes. Because the implications of short-duration, non-uniform metamorphism for the nature of tectonic processes are so profound (e.g., Lister et al., 2001), there exists a need for new geochronological methods that are capable of assessing these claims of short-duration, non-uniform regional metamorphism.

Attempts to use high-precision geochronology to decipher time scales of metamorphism began with methods involving direct dating of garnet growth using the Lu–Hf, Rb–Sr and Sm–Nd systems (e.g., Christensen et al., 1989, 1994; Vance and O'Nions, 1990, 1993; Oliver et al., 2000; Baxter et al., 2002; Lagos et al., 2007; Lancaster et al., 2008; Herwartz et al., 2011). More-recent development of improved microsampling (e.g., Ducea et al., 2003, Johnston et al., 2007; Pollington and Baxter, 2011) and differential geochronology techniques that use Lu–Hf and Sm–Nd zoning and ages (e.g., Lapen et al., 2003; Skora et al., 2006; Kylander-Clark et al., 2007; Kohn, 2009) have enabled high-precision dating of discrete portions of individual garnet grains. These approaches have allowed recognition of metamorphic episodes as short as ~10^6 yr within crystal growth periods spanning ~10^6–10^7 yr (e.g., Pollington and Baxter, 2010, Dragovic et al., 2012).

The time-consuming nature of garnet microdrilling and thermal ionization mass spectrometry (TIMS) analysis inhibits procurement of large datasets. Laser-ablation inductively coupled-plasma mass spectrometry (LA-ICP-MS), however, allows rapid in situ analysis and enables production of vast datasets that may be used to resolve individual age groupings that only emerge when population size becomes significantly large (e.g., Spencer et al., 2013; Pullen et al., 2014). LA-ICP-MS is especially well suited to U/Th–Pb dating of monazite and zircon,

---

[*] Corresponding author at: Department of Earth Sciences, Durham University, South Rd, Durham DH1 3LE, Durham, UK.
E-mail addresses: daniel.viete@durham.ac.uk, daniel.viete@gmail.com (D.R. Viete).

http://dx.doi.org/10.1016/j.chemgeo.2015.09.013
0009-2541/

which can provide high-precision dates due to their relatively high U or Th content and low common Pb. Additionally, the relatively low diffusivities of Pb in monazite and zircon offer confidence that U/Th–Pb ages obtained from these minerals reflect (re)crystallization or precipitation rather than diffusive resetting, even for temperatures in excess of 700 °C (Cherniak and Watson, 2003; Cherniak et al., 2004).

Qualitative and semi-quantitative techniques for linking accessory mineral dates to petrological context or pressure–temperature (P–T) conditions have been developed in recent years. The petrological context for zircon and monazite (re)crystallization during metamorphism can be related to the presence of garnet/xenotime through qualitative interpretation of HREE (and Y) patterns and/or abundances (e.g., Rubatto et al., 1999, 2009; Foster et al., 2000, 2002; Hoskin and Ireland, 2000; Rubatto, 2002; Hermann and Rubatto, 2003; Hoskin and Schaltegger, 2003; Baldwin et al., 2004; Kohn et al., 2005) and plagioclase through Eu abundance relative to that of neighboring REEs (e.g., Schaltegger et al., 1999; Hoskin and Ireland, 2000; Belousova et al., 2002; Rubatto, 2002). 'Petrochronology' has been used to refer to techniques that use simultaneous measurement of isotope ratios and trace-element abundances in accessory minerals. These techniques include laser ablation split-stream ICP-MS (LASS) approaches that simultaneously analyze a single stream of laser-ablated material with two ICP-MS: one for geochronology, and one for trace-element analysis (e.g., Yuan et al., 2008; Chen et al., 2010; Donaldson et al., 2013; Kylander-Clark et al., 2013).

High-precision, petrologically controlled U–Pb zircon geochronology has been successful in extracting information on young, short-duration metamorphic episodes (e.g., Gasser et al., 2012; Rubatto et al., 2013; Chen et al., 2015). These studies have used conventional secondary ion mass spectrometry (SIMS) or LA-ICP-MS analyses of sectioned zircons. Using these approaches, distinct metamorphic events over time scales of 10^6–10^7 yr can be resolved. However, as noted above, to test the validity of the metamorphic time scale estimates of 10^4–10^6 yr being obtained from diffusion modeling, advances in high-precision geochronology must allow time scale resolutions of $<10^6$ yr. New surface analysis techniques may hold the key to such advances.

Geochronology by surface analysis began with depth-profiling studies that used SIMS dating techniques (e.g., Grove and Harrison, 1999; Carson et al., 2002; Mojzsis and Harrison, 2002; Breeding et al., 2004; Trail et al., 2007; Abbott et al., 2012; Vorhies et al., 2013). More recently, LA-ICP-MS has also been used for depth profiling. Studies employing LA-ICP-MS use either continuous-pulse (e.g., Plotnikov et al., 2001; Woodhead et al., 2004; Johnston et al., 2009; Kohn and Corrie, 2011; Smye and Stockli, 2014; Kelly et al., 2014) or single-pulse techniques (Cottle et al., 2009, 2012; Steely et al., 2014; Stearns et al., in review). The single-shot technique presents some significant obstacles to extraction of reliable data (Cottle et al., 2009, 2012), but offers the advantage of using significantly smaller volumes of material (i.e. smaller shot depth) for each date.

Single-shot (SS-)LA-ICP-MS depth profiling offers two distinct advantages over other U–Pb methods. First, the small volume of analyte needed for SS-LA-ICP-MS depth profiling results in less mixing of different depths within the crystal, providing better spatial resolution. SS-LA-ICP-MS depth profiling is capable of resolving an order of magnitude smaller variation than can be sampled by LA-ICP-MS on sectioned grains (e.g., Cottle et al., 2009, 2012); this also makes grains with rims thinner than laser spot diameter tenable for analysis. Second, the SS-LA-ICP-MS surface analysis method is quick (~3–6 min per grain) and relatively inexpensive, allowing collection of the vast datasets required to confidently resolve short-duration metamorphic age populations (e.g., Pullen et al., 2014).

In this contribution we present a new approach for single-shot laser-ablation split-stream inductively coupled-plasma mass spectrometry (SS-LASS). The approach offers distinct advantages over current methods in high-precision U–Pb geochronology for recognizing multiple, short-duration (re)crystallization events. We use the technique to resolve multiple episodes of short-duration zircon (re)crystallization in the Venezuelan Cordillera de la Costa, between 33 and 18 Ma, with a resolution of 500 kyr or less.

2. The Caribbean Mountain System

The Caribbean Mountain System (Menéndez, 1966) defines part of the boundary between the Caribbean and South American Plates. The system stretches 1400 km E–W, from the Santa Marta Massif and Guajira Peninsula, Colombia to northern Trinidad (Fig. 1). It consists of four distinct lithotectonic units: i) the Cordillera de la Costa; ii) Caucagua–El Tinaco belt; iii) Paracatos belt, and iv) Villa de Cura belt (Fig. 1; Menéndez, 1966). These four elements form the hinterland of an orogen that includes the Serranía del Interior foreland fold-and-thrust belt farther south (Fig. 1; Avé Lallemant, 1997). The Caribbean Mountain System's current arrangement reflects Miocene and younger juxtaposition of discrete lithotectonic units in a dextral strike-slip setting (Avé Lallemant, 1997).

2.1. Cordillera de la Costa

The Cordillera de la Costa is a coastal belt bounded by two major dextral strike-slip faults, the San Sebastian Fault and the La Victoria Fault (Menéndez, 1966; Fig. 1). The Cordillera de la Costa consists of Paleozoic orthogneiss and schist overlain by Mesozoic siliciclastic rocks and then graphitic mica schists, calc-schists, marbles and quartzites that host eclogite, blueschist and garnet amphibolite (Ostos et al., 2005; Ostos and Sisson, 2005).

Eclogite, blueschist and garnet amphibolite (with MORB protoliths) blocks in continentally derived gneiss, schist, marble and quartzite occur in the Franja Costera unit of the northern Cordillera de la Costa (e.g., Stephan, 1985; Bellizia and Dengo, 1990; Avé Lallemant, 1997; Giunta et al., 2002; Ostos and Sisson, 2005; Sorensen et al., 2005). These are best exposed around Puerto Cabello (Fig. 1), where a steeply dipping mélange consisting of highly deformed graphitic mica schists, calc-schists, gneisses, marbles and quartzites hosts 10^{-2}–10 m-sized eclogite, blueschist and garnet amphibolite lenses (e.g., Morgan, 1970; Sisson et al., 1997). Mineral stretching lineations and well-developed shear-sense indicators in the schists and mylonites at Puerto Cabello attest to high shear strain during development of the mélange. At least five generations of deformation relating to an early, syn-metamorphic 'orogenic phase' have been recognized, as well as two generations of deformation relating to a second 'orogenic phase' that did not involve extensive metamorphism (Avé Lallemant and Sisson, 2005).

Similar rocks crop out on Isla Margarita (Fig. 1), where eclogite and amphibolite blocks are also hosted within a mélange of continentally derived metasediments (Blackburn and Navarro, 1977; Maresch and Abraham, 1981; Bocchio et al., 1996). The origins of the Isla Margarita and Puerto Cabello eclogites are often linked (Bellizia and Dengo, 1990; Avé Lallemant, 1997), however, the peak P–T conditions (Sisson et al., 1997), fluid histories (Sorensen et al., 2005) and cooling histories (Sisson et al., 2005) are different.

2.1.1. Conditions and timing of metamorphism

Building on earlier work by Morgan (1970), Sisson et al. (1997) used garnet–clinopyroxene thermometry, jadeite barometry and Si-in-phengite thermobarometry to estimate formation of the Puerto Cabello eclogites at ~650–700 °C and >1.5 GPa, and the subsequent garnet-amphibolite-facies overprint at ~400–500 °C and <1.5 GPa. The co-existence of kyanite and glaucophane in pelitic schists adjacent to the eclogite blocks at Puerto Cabello suggests that the entire mélange experienced high-pressure metamorphism at >630 °C and >2.2 GPa, however, garnet–muscovite–biotite–plagioclase thermobarometry on pelitic schists returned lower P–T conditions of ~450–520 °C and ~1.8 GPa (Sisson et al., 1997). Thermobarometry shows that the eclogites of Isla Margarita

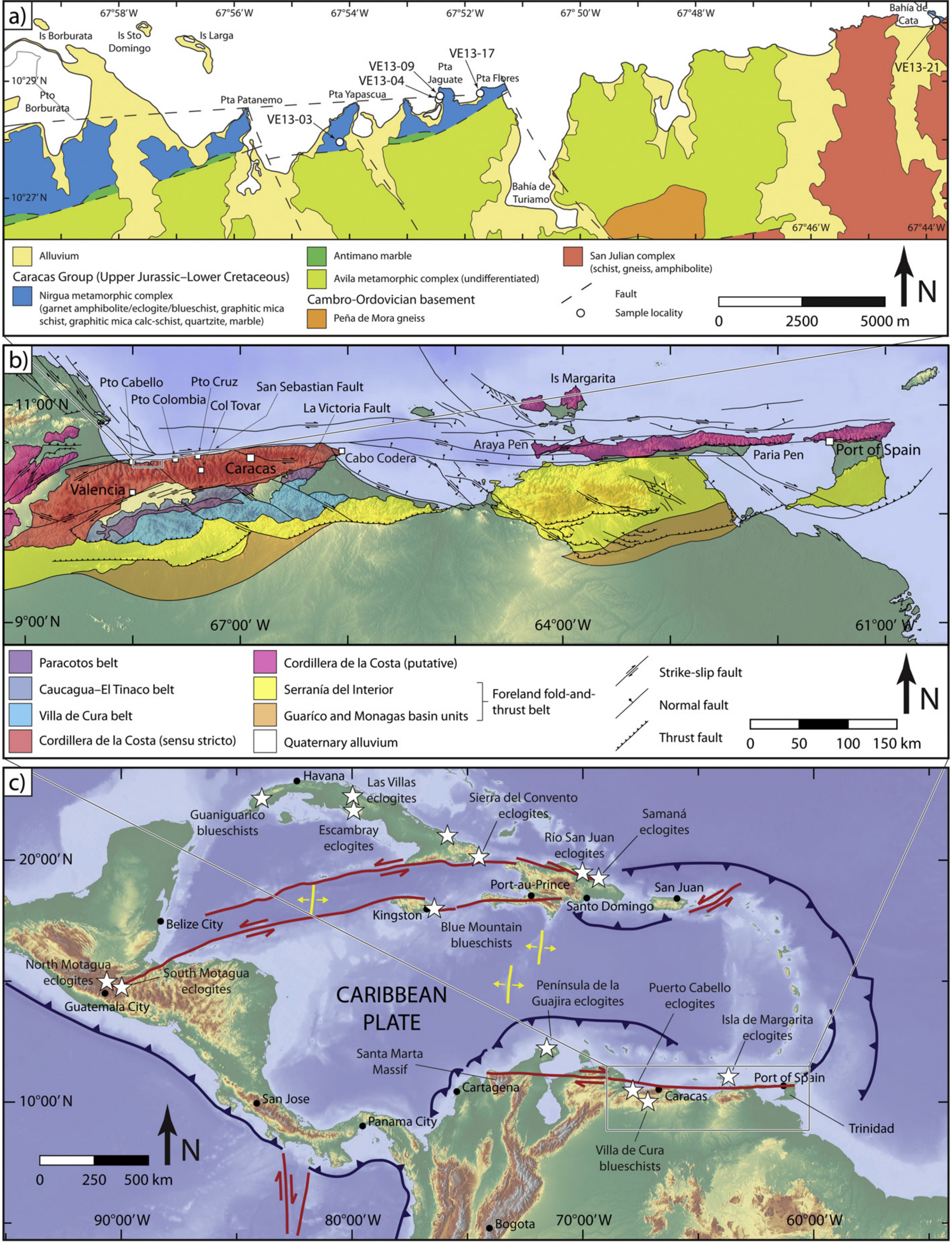
a)
67°58′W
67°56′W
67°54′W
67°52′W
67° 50′W
67°48′W
67°46′W
67°44′W
10°29′N
10°27′N
Is Borburata
Is Sto Domingo
Is Larga
Pto Borburata
Pta Patanemo
Pta Yapascua
Pta Jaguate
Pta Flores
VE13-03
VE13-04
VE13-09
VE13-17
VE13-21
Bahía de Cata
Bahía de Turiamo
Alluvium
Caracas Group (Upper Jurassic–Lower Cretaceous)
Nirgua metamorphic complex (garnet amphibolite/eclogite/blueschist, graphitic mica schist, graphitic mica calc-schist, quartzite, marble)
Antimano marble
Avila metamorphic complex (undifferentiated)
Cambro-Ordovician basement
Peña de Mora gneiss
San Julian complex (schist, gneiss, amphibolite)
Fault
Sample locality
N
0
2500
5000 m
b)
11°00′N
9°00′N
67°00′ W
64°00′W
61°00′ W
Pto Cabello
Pto Colombia
Pto Cruz
Col Tovar
San Sebastian Fault
La Victoria Fault
Is Margarita
Cabo Codera
Caracas
Valencia
Araya Pen
Paria Pen
Port of Spain
Paracotos belt
Caucagua–El Tinaco belt
Villa de Cura belt
Cordillera de la Costa (sensu stricto)
Cordillera de la Costa (putative)
Serranía del Interior
Guaríco and Monagas basin units
Foreland fold-and-thrust belt
Quaternary alluvium
Strike-slip fault
Normal fault
Thrust fault
N
0
50
100
150 km
c)
Havana
Guaniguarico blueschists
Las Villas eclogites
Escambray eclogites
Sierra del Convento eclogites
Río San Juan eclogites
Samaná eclogites
20°00′N
10°00′N
Port-au-Prince
Santo Domingo
San Juan
Kingston
Blue Mountain blueschists
Belize City
North Motagua eclogites
South Motagua eclogites
Guatemala City
CARIBBEAN PLATE
Península de la Guajira eclogites
Puerto Cabello eclogites
Isla de Margarita eclogites
Santa Marta Massif
Cartagena
Caracas
Port of Spain
Trinidad
Villa de Cura blueschists
San Jose
Panama City
Bogota
N
0
250
500 km
90°00′W
80°00′W
70°00′W
60°00′W

experienced high-pressure/low-temperature (HP/LT) metamorphism at conditions of ~525–650 °C and 1.3–1.9 GPa (Blackburn and Navarro, 1977; Maresch and Abraham, 1981; Bocchio et al., 1996). Knowledge on the timing of metamorphism of the Cordillera de la Costa is limited to c. 76 Ma and 43–28 Ma K–Ar/Ar–Ar amphibole and mica dates, and 49–42 Ma and 24–14 Ma fission-track apatite and zircon dates (Table 1).

2.2. Sample descriptions

Four metasedimentary rocks (a quartzite, omphacitite, graphitic mica schist and graphitic mica calc-schist) and one orthogneiss were analyzed in this work. All were sampled from a high-strain mélange that crops out on the north-central Venezuelan coast, between Puerto Cabello and Puerto Colombia (Fig. 1). The samples were chosen to represent the variety of zircon-bearing lithologies that form the mélange. All rocks experienced amphibolite-facies metamorphism, which followed eclogite-facies metamorphism in at least one sample (the omphacitite). Evidence of greenschist-facies retrogression is also present in some samples. Descriptions and photomicrographs of each sample are provided in the Supplementary material.

3. Methods

To assess the (poly)metamorphic history of the Cordillera de la Costa, we used a combination of continuous-pulse LASS on zircon and titanite in thin sections, and SS-LASS on zircon grains mounted in epoxy.

Zircon grains in thin section were imaged using cathodoluminescence (CL) and combined secondary/back-scattered electron (BSE) microscopy on the FEI Quanta 400f field-emission source scanning electron microscope (SEM) at the Department of Earth Science, University of California Santa Barbara (UCSB). Titanite grains in thin section were imaged using BSE microscopy.

Approximately 200 zircons were handpicked from each sample following crushing, and magnetic, and density separation. The zircons were laid flat on their largest face on a piece of packing tape pulled taut over glass, to ensure a flat mounting surface. After potting in epoxy, the surface was cleaned with ethanol and isopropyl alcohol, but not polished.

3.1. Laser ablation split-stream ICP-MS (LASS)

Measurements were made using the LASS petrochronology system at UCSB (Kylander-Clark et al., 2013). U/Th–Pb measurements used a Nu Plasma HR-ES MC-ICP-MS, with a collector arrangement that permits simultaneous measurement of ^{238}U and ^{232}Th on Faraday cups with 10^{11} Ω resistors, and ^{208}Pb, ^{207}Pb, ^{206}Pb and ^{204}Pb + ^{204}Hg on ETP ion counters. Trace-element analyses were performed on an Agilent 7700x quadrupole ICP-MS with the S-option and a second backing pump. The samples were ablated with a Photon Machines Analyte 193 nm ArF laser system, equipped with a low-volume HelEx ablation cell modified from the design of Eggins et al. (1998, 2005). High-purity He flow through the ablation cell carried the analyte to a mixing bulb where the aerosol was mixed with Ar. The aerosol stream was then split, with approximately half of the analyte fed to each of the mass spectrometers.

For data reduction, ^{235}U/^{207}Pb was calculated from measured values of ^{238}U/^{206}Pb and ^{207}Pb/^{206}Pb, assuming a constant ^{238}U/^{235}U value of 137.88 (Steiger and Jäger, 1977). The U decay constants of Jaffey et al. (1971) and the Th decay constants of Amelin and Zaitsev (2002) were used in calculation of all ages. Isoplot 3.75 was used for production of all ^{238}U/^{206}Pb v. ^{207}Pb/^{206}Pb (Tera–Wasserburg) concordia diagrams and probability density distribution plots. All isochron (and '^{207}Pb-corrected' ^{238}U/^{206}Pb) ages for the zircon data were anchored to common ^{207}Pb/^{206}Pb values of Stacey and Kramers (1975) for the age obtained. Due to significant spread in ^{206}Pb in the titanite data, titanite isochron dates were not anchored. Uncertainties on all dates from this study are quoted at the 95% confidence level. The continuous-pulse LASS and SS-LASS data are given in the Supplementary material.

3.1.1. U–Pb zircon SS-LASS

Analyte was obtained by single-shot laser ablation, with the laser operating in 'high voltage' mode at 12–13.2 kV, as required to achieve a laser fluence of 4 J cm^{-2}. Each SS-LASS analysis (including cleaning shots) samples an ~100 nm layer of zircon (Cottle et al., 2009, 2012; Kylander-Clark et al., 2013). Consecutive analyses were separated by a 12 s pause. For each grain, a single 53 μm-diameter cleaning shot was followed by 10 discrete (single-shot) analyses using a 41 μm-diameter spot. The ~100 nm cleaning shot is necessary to mitigate the effects of surface contamination, but also alpha recoil, which occurs over distances of tens of nm and is most likely to disturb isotope systematics at the grain edge (Romer, 2003). Final ablation pit depths for each zircon were ~1–2 μm (as determined by SEM and optical microscopy). Every seven analyses were bracketed by zircon reference materials Plešovice (^{238}U/^{206}Pb age of 337.13 ± 0.37 Ma: Sláma et al., 2008), GJ1 (^{238}U/^{206}Pb age of 601.7 ± 1.3 Ma: Jackson et al., 2004; Kylander-Clark et al., 2013) and 91500 (^{238}U/^{206}Pb age of 1062.4 ± 0.4 Ma: Wiedenbeck et al., 1995). Reference material analyses were performed on polished fragments located on a separate mount to the unknowns. For all analyses, distances between reference materials and unknowns were kept to a minimum practicable value, so as to minimize analytical bias relating to sample position. A total of 63–84 unknown zircon grains and 27–36 reference material spots were analyzed per sample.

Data reduction followed the methods of Cottle et al. (2009, 2012). All of the data for secondary reference material GJ1 returned ^{206}Pb/^{238}U and ^{207}Pb/^{206}Pb ratios with an MSWD value too high for the data to be a single population (Wendt and Carl, 1991) (see Supplementary material); the same was observed for the Plešovice secondary reference material. If GJ1 and Plešovice are isotopically homogeneous, this finding indicates that the calculated uncertainty is an underestimate. An external error was thus added in quadrature to the internal uncertainty of the secondary reference materials until the MSWD for each of the ^{206}Pb/^{238}U and ^{207}Pb/^{206}Pb ratios was consistent with a single population (see Wendt and Carl, 1991); this error is 5% (for both ^{206}Pb/^{238}U and ^{207}Pb/^{206}Pb) and was also added in quadrature to the internal uncertainty for all unknowns. The isochron dates for GJ1 and Plešovice derived from this method are accurate to within 1.5% of published values.

Elemental Th and U concentrations were obtained by reference to 91500 zircon; the calculated abundances of these elements in secondary reference material GJ1 (Th = 10.5 ± 2.7 ppm, U = 303 ± 70 ppm) match published values (Th = 9.0 ppm, U = 308 ppm: Liu et al., 2010; Kylander-Clark et al., 2013). 2σ uncertainty on the trace-element measurements made by MC-ICP-MS are on the order of ~25%.

The small volume of analyte (and transient signal at the ICP-MS) produced in the SS-LASS approach limits the number of elements that can be analyzed for each laser ablation shot. This is an inherent tradeoff of the SS-LASS technique: enhanced spatial resolution is traded for

Fig. 1. Maps of: a) localities for the samples in this study and geology of the coastal Cordillera de la Costa in the region east of Puerto Cabello; b) regional geology of northern Venezuela and Trinidad showing the lithotectonic units of the Caribbean Mountain System and associated fold-and-thrust belt, and c) tectonics of the Caribbean showing locations of plate boundaries (subduction zones: blue, strike-slip boundaries: red, spreading ridges: yellow) and high-pressure/low-temperature metamorphic rocks (white stars). After Ysaccis (1997), Audemard et al. (2000), Urbani et al. (2002).

Table 1

Summary of geochronological and thermochronological constraints from selected units of the Coastal Mountain System of eastern Colombia and Venezuela.

Location and rock unit	Approximate location	U–Pb age ± 2σ (Ma)	K–Ar/Ar–Ar age ± 2σ (Ma)	Fission-track age ± 2σ (Ma)
Cordillera de la Costa				
Autopista Valencia–Puerto Cabello				
Guaremal gneiss	10°21′42″N, 68°05′31″W	501 ± 25 (Zrn)[8]	–	19.8 ± 2.4 (Zrn)[8] 16.3 ± 3.2 (Ap)[8]
Guaremal granite	10°19′38″N, 68°05′32″W	–	33 ± 4 (Bt)[1] 32 ± 4 (Bt)[1] 31 ± 3.6 (Bt)[1]	19.8 ± 2.4 (Zrn)[8] 15.0 ± 2.8 (Ap)[8]
Mica schist in Avila Formation	10°20′58″N, 68°06′32″W	–	42.3 ± 0.6 (Ms)[8]	–
mica schist in Avila Formation	10°18′92″N, 68°05′23″W	–	34.2 ± 0.4 (Ms)[8]	–
mica schist in Avila Formation	10°19′28″N, 68°05′28″W	–	28.0 ± 0.4 (Ms)[8]	–
Colonia Tovar and Puerto Cruz				
Tinaco diorite/gneiss		–	–	49.0 ± 5.8 (Zrn)[2] 43.4 ± 5.6 (Zrn)[2] 41.9 ± 4.9 (Zrn)[2]
Tovar granite/gneiss		–	–	16.4 ± 2.1 (Zrn)[2]
Parque Nacional El Avila (east)				
Oritapo diorite		–	77 ± 8.0 Ma (Bt)[1] 76 ± 7.8 Ma (Bt)[1]	–
Parque Nacional El Avila (west)				
Metasediment in Caracas Group		–	32.9 ± 0.6 Ma (Ms)[7]	–
Peña de Mora gneiss		–	–	23.9 ± 1.7 (Zrn)[2] 18.9 ± 1.9 (Zrn)[2] 18.8 ± 2.1 (Zrn)[2] 18.4 ± 1.9 (Zrn)[2] 17.5 ± 1.7 (Zrn)[2] 17.4 ± 2.1 (Zrn)[2]
Parque Nacional Henri Pittier				
actinolite schist	10°21′20″N, 67°36′57″W	–	37 ± 6 Ma (Act)[8]	–
Choroní granite	10°18′20″N, 67°36′58″W	471 ± 23 (Zrn)[8]	30 ± 3.8 Ma (Bt)[1] 30 ± 3.6 Ma (Bt)[1]	13.6 ± 2.8 (Zrn)[8] 14.1 ± 2.8 (Ap)[8]
Choroní granite		–	–	24.1 ± 3.0 (Zrn)[2] 22.3 ± 2.3 (Zrn)[2] 21.9 ± 2.9 (Zrn)[2] 17.5 ± 1.9 (Zrn)[2]
Trondhjemitic dyke within quartzofeldspathic schist at Bahía de Cata	10°29′43″N, 67°45′10″W	511 ± 2 (Zrn)[8]	–	–
Puerto Cabello				
Garnet amphibolite in Nirgua Complex		–	32.4 ± 2.4 (Amph)[3]	–
Mica schist in Avila Formation	10°28′02″N, 67°55′53″W	–	42.6 ± 0.6 (Ms)[8]	–
Guajira Peninsula				
Guajira eclogite (clast from Miocene basal conglomerate, Etpana Terrane)	12°17′00″N, 71°41′00″W	–	82.2 ± 5.0 (Ms)[10]	–
Guajira eclogite (clast from Miocene basal conglomerate, Etpana Terrane)	12°17′00″N, 71°41′00″W	–	79.2 ± 2.2 (Ms)[10]	–
Isla Margarita				
Amphibolite in La Rinconda Group	11°03′48″N, 64°00′16″W	–	62.3 ± 2.8 (Hbl)[8]	–
Eclogite in Juan Griego Group	11°01′45″N, 63°52′12″W	c. 100–90 (cross-cutting relationships)[9]	92.4 ± 1.0 (Act)[8]	–
El Salado metagranite		c. 86–85 (Zrn)[9]	–	c. 53–50 (Zrn)[4]
Guayacán gneiss		c. 116–106 (Zrn)[9]	–	–
Garnet amphibolite in Juan Griego Group	11°09′22″N, 63°53′50″W	–	52.8 ± 0.4 (Bar)[8]	–
Macanao orthogneiss		271.0 ± 6.6 (Zrn)[9]	–	–
Matasiete metatrondhjemite		c. 114 (Zrn)[9]	72 ± 12 (Amph)[1]	c. 53–50 (Zrn)[4]
Metaconglomerate in La Rinconda Group	11°04′00″N, 64°00′10″W	–	65.0 ± 0.4 (Ms)[8] 39.8 ± 0.2 (Bt)[8]	–
Mica schist in La Rinconda Group	11°02′48″N, 64°00′29″W	–	68.3 ± 0.4 (Ms)[8] 24.9 ± 1.8 (Bt)[8]	–
Mica schist in Los Robles Group	10°59′49″N, 63°51′22″W	–	53.5 ± 1.4 (Ms)[8]	–
Quartzofeldspathic schist in La Rinconda Group	11°00′20″N, 63°52′29″W	–	88.0 ± 0.6 (Ms)[8]	–
Araya Peninsula				
Mica schist in Tunapui Formation	10°37′00″N, 64°03′30″W	–	90.8 ± 0.8 (Ms)[8]	–
Garnet–staurolite schist in Manicuare Formation	10°35′00″N, 63°20′00″W	–	84.8 ± 0.4 (Ms)[8] 45.1 ± 0.6 (Bt)[8]	–
Paria Peninsula				
Dragon gneiss	10°43′42″N, 61°52′33″W	321 + 13/−29 (Zrn)[5]	23.3 ± 0.4 (Ms)[5]	–
Villa de Cura belt				
Glaucophane–epidote subbelt		–	78.5 ± 1.0 (Ms)[6]	–
Barroisite subbelt		–	96.8 ± 1.8 (Bar)[6] 91.1 ± 1.0 (Ms)[6] 89.9 ± 1.2 (Stp)[6]	–
Barroisite subbelt		–	90.1 ± 1.2 (Ms)[6]	–

Table 1 (*continued*)

Location and rock unit	Approximate location	U–Pb age ± 2σ (Ma)	K–Ar/Ar–Ar age ± 2σ (Ma)	Fission-track age ± 2σ (Ma)
Barroisite subbelt		–	96.3 ± 0.8 (Bar)[6] 89.5 ± 1.2 (Ms)[6]	–

Some locations are shown on the regional geological map of Fig. 1. References: 1: Santamaría and Schubert (1974), 2: Kohn et al. (1984), 3: Loubet et al. (1985), 4: Stöckhert et al. (1995), 5: Speed et al. (1997), 6: Smith et al. (1999), 7: Speed (pers. Comm.) reported in Sisson et al. (2005), 8: Sisson et al. (2005), 9: Maresch et al. (2009), 10: Weber et al. (2011). Act: actinolite, Amph: amphibole, Ap: apatite, Bar: barroisite, Bt: biotite, Ms: muscovite, Stp: stilpnomelane, Zrn: zircon.

reduced chemical information. SS-LASS analyses of this study monitored two trace elements by quadrupole ICP-MS. In the first session, Ti was chosen as a potential indicator of zircon (re)crystallization temperature and Y was analyzed as a proxy for garnet crystallization/breakdown. In later sessions, Eu was analyzed—as a proxy for plagioclase crystallization/breakdown—instead of Ti.

Elemental concentrations of Ti, Y and Eu were measured from ^{49}Ti, ^{89}Y, and ^{153}Eu, using zircon 91500 (Wiedenbeck et al., 2004; Yuan et al., 2008; Liu et al., 2010; Kylander-Clark et al., 2013) as the reference material (see Supplementary material). Counting times were 0.06 s, 0.03 s and 0.06 s per sweep for ^{49}Ti, ^{89}Y and ^{153}Eu, respectively.

The peak identification and pulse signal integration routine of *SLaPChron* (Cottle et al., 2012) was used to extract a single, total-signal count for ^{49}Ti, ^{89}Y and ^{153}Eu from the quadrupole ICP-MS output for each single-shot analysis. Elemental abundances for Eu, Ti and Y were assumed to be linearly proportional to these count values; no downhole fractionation correction was applied for the Eu, Ti and Y abundance calculations. The values for Eu (0.92 ± 0.20 ppm), Ti (3.9 ± 1.9 ppm) and Y (259 ± 45 ppm) for secondary reference material GJ1 are all accurate (Eu = 0.93 ppm, Ti = 3.6 ppm, Y = 252 ppm: Liu et al., 2010; Kylander-Clark et al., 2013), supporting the assumption of linear proportionality between elemental abundance and total counts, and demonstrating negligible influence of downhole fractionation. The statistical uncertainty on values obtained for Eu and Y concentration in GJ1 suggests that 2σ uncertainties on trace-element measurements made by the quadrupole ICP-MS are on the order of ~20% (the Ti population was too small to provide meaningful statistics).

3.1.2. U–Pb titanite and zircon continuous-pulse LASS

Conventional, continuous-pulse LASS analyses were performed on zircon and titanite in thin sections of VE13-04 and VE13-09. Laser ablation for each analysis involved 80 consecutive laser shots at a frequency of 4 Hz, performed in 'energy stability' mode with a laser fluence setting of 4 J cm^{-2}. Analyses were separated by a 15 s pause. Zircon analyses used a 14.5 μm-diameter spot. Prior to each analysis, two cleaning shots were performed using a 21 μm-diameter spot. 91500 and GJ1 were used as primary and secondary reference materials, respectively, with 4–6 unknowns analyzed between each set of reference material analyses. Titanite analyses used a 41 μm-diameter spot, with two 53 μm-diameter cleaning shots performed prior to each analysis. BLR (1047.4 ± 1.4 Ma: Aleinikoff et al., 2007) was used as the primary isotope reference material and P5701G (390.9 ± 1.1 Ma; Kylander-Clark et al., 2008) or Y1710C5 (388.6 ± 0.5 Ma: Spencer et al., 2013) as the secondary isotope reference material. NIST 610 glass (Pearce et al., 1997) was used as the trace-element reference material and Ca was used as the internal standard. All titanite analyses for VE13-04 and VE13-09 were made in one run for each rock. Trace-element concentrations were measured on the quadrupole ICP–MS, for both VE13-04 and VE13-09; instrumentation problems prevented recovery of the trace-element data for VE13-09.

U/Th–Pb isotope ratios and elemental abundances and uncertainties were calculated using Iolite v3 and following the data reduction with downhole fractionation-correction method of Paton et al. (2010). An external error of 2% was added in quadrature to the uncertainties on zircon U–Pb isotope ratios obtained following data reduction, producing agreement between ages obtained for the secondary reference material (GJ1) and published values (Jackson et al., 2004; Kylander-Clark et al., 2013). The same 2% uncertainty was added in quadrature to the individual titanite U–Pb ratio values, producing an MSWD of 0.13 and 0.47 for the best-fit ^{238}U/^{206}Pb v. ^{207}Pb/^{206}Pb isochrons of VE13-04 and VE13-09, respectively. These low MSWD values indicate that 2% is excessive; values of 0.6% for VE13-04 and 1.2% for VE13-09 are sufficient to achieve MSWD ≈ 1.

4. Results

Most of the zircons (Fig. 2) have oscillatory zoning, indicating an original igneous parentage. These zoned regions define zircon cores that are typically rounded to subrounded, and some are offset from the grain centers; both features are compatible with sedimentary transport. Other grains have sector-zoned cores, which may indicate metamorphic (e.g. Schaltegger et al., 1999) or low-temperature/slow-cooling igneous (e.g. Watson and Liang, 1995; Hoskin and Schaltegger, 2003; Chamberlain et al., 2014) origin. These sector-zoned cores show no features compatible with sedimentary transport. Most zircons are rimmed by thin (<5 μm, generally <1 μm), faceted/idioblastic CL-dark overgrowths. The rim/core boundaries are either: i) sharp and curviplanar, suggesting that the rim is a metamorphic overgrowth, or ii) diffuse or dentate, compatible with the rim forming by dissolution–precipitation of existing zircon.

Zircons from VE13-04 are associated with albite + Na–Ca amphibole symplectite (Fig. 2), suggesting that zircon overgrowth occurred under amphibolite-facies conditions. Albite + Na–Ca amphibole symplectite overprints radial cracks in the omphacite that encloses zircon (Fig. 2); this feature is consistent with significant decompression from omphacite-stable (eclogite-facies) conditions prior to zircon overgrowth. The context(s) for zircon overgrowth in the other samples are less clear. Transmitted-/reflected-light images of zircon grains from each sample are provided in the Supplementary material. The zircon grains, when viewed under transmitted/reflected light, display no evidence of metamict domains.

Titanite grains in VE13-04 surround rutile (Fig. 3), indicating formation from rutile breakdown. Albite + Na–Ca amphibole symplectite along omphacite grain boundaries occurs in the vicinity of titanite (Fig. 3), suggesting amphibolite-facies titanite growth in VE13-04. Metamorphic context for titanite growth in VE13-09 is ambiguous.

4.1. SS-LASS

The isotopic ratios of each laser shot are given in the Supplementary material, and example Tera–Wasserburg diagrams are shown in Fig. 4. Most grains display systematic downhole changes in isotopic ratios. The first shots generally have the most common Pb (e.g., VE13-03 zircon 16, VE13-04 zircon 43, VE13-17 zircon 18), likely due to surface contamination. In all grains, earlier shots have younger or equivalent ^{207}Pb-corrected ^{206}Pb/^{238}U dates than/to later shots. The majority of grains display a smooth transition in ^{207}Pb/^{206}Pb and ^{238}U/^{206}Pb ratios, most typically from young rim analyses with lower radiogenic/common Pb to old, more-radiogenic core analyses. In some grains the youngest data define a multi-point isochron (e.g., VE13-04 zircon 43), whereas in other grains the oldest data define a multi-point isochron (e.g., VE13-09 zircon 59). All the examples in Fig. 4 have analyses with

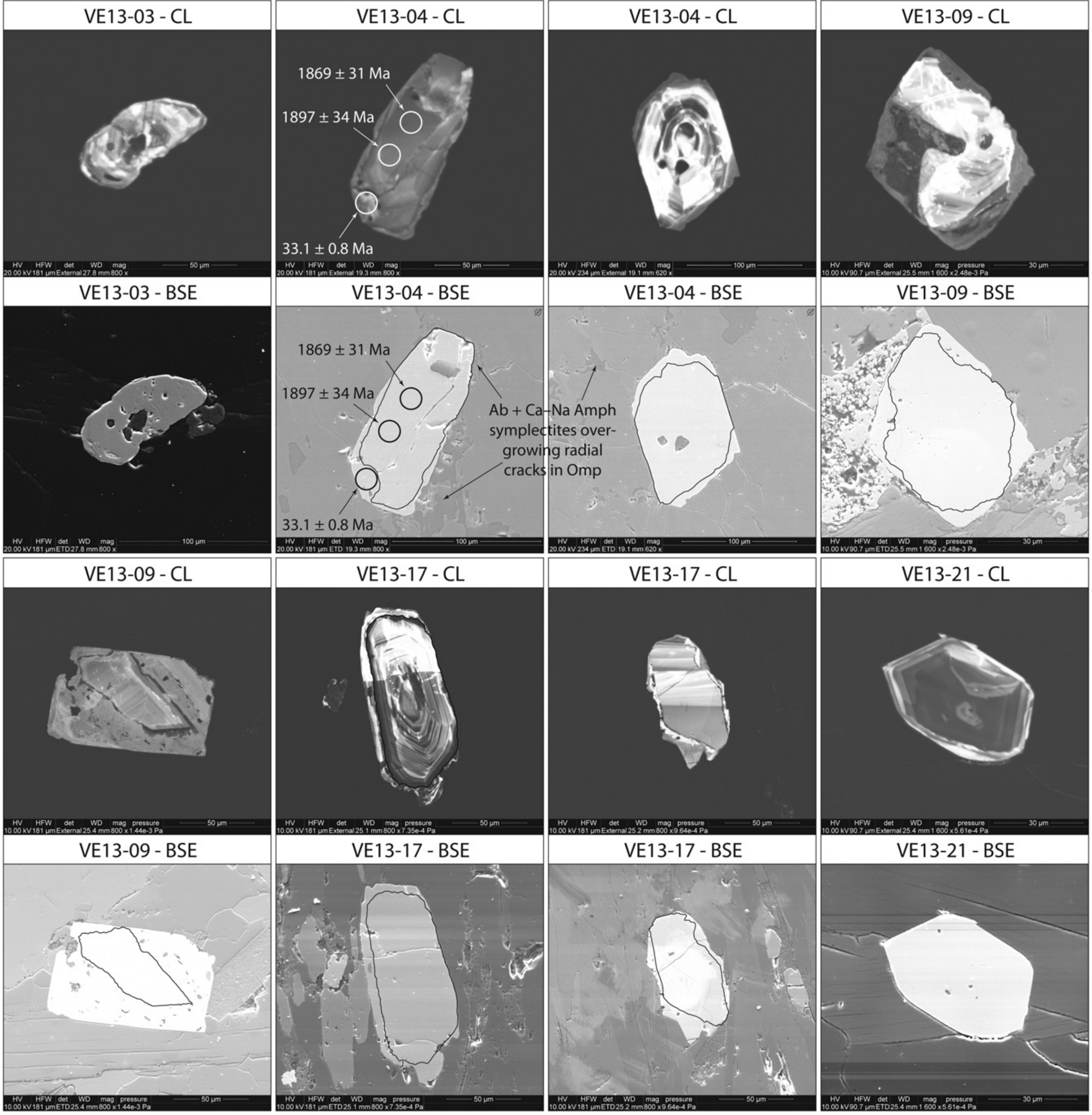

Fig. 2. CL and combined SE/BSE images of selected zircon grains from the rocks analyzed. Core–rim boundaries for some grains are indicated by black outline on BSE images. Continuous-pulse LASS spots shown for VE13-04 are labeled with ^{207}Pb-corrected ^{238}U/^{206}Pb dates. Amph: amphibole, Omp: omphacite.

isotopic ratios intermediate between the young and old endmembers; these may be: i) laser-induced, mechanical mixtures of young rim material and old core material, or ii) progressively younging rims grown on old core material.

Dates older than 125 Ma were assumed to be inherited ages because peri-Caribbean HP/LT metamorphism occurred during or after the Aptian subduction polarity reversal that produced the Caribbean Arc (e.g., Pindell et al., 2005, 2006). Of the 63 grains analyzed from VE13-21 (Cata orthogneiss), 11 grains yielded discrete populations of dates older than 125 Ma. These 11 populations are defined by analyses from the deepest parts of the ablation pits (i.e. the last four-to-10 single-shot analyses performed). Considered together, the 67 analyses that form the 11 discrete populations give an isochron of 493.2 ± 7.4 Ma (MSWD = 1.7; Fig. 5). The MSWD value is slightly greater than what would be expected for a single population (MSWD < 1.36; Wendt and Carl, 1991). This may indicate episodic/protracted zircon crystallization (slow cooling) during the Late Cambrian, consistent with the sector zoning observed in zircon cores (Fig. 2).

Analyses younger than 125 Ma were considered in two different ways: i) if > 21 Ma, as isochrons defined by two or more SS-LASS analyses anchored to common Pb, or ii) if < 21 Ma, as ^{207}Pb-corrected ^{206}Pb/^{238}U dates (Table 2). In the case of the isochrons, we applied a minimum of 1.5% uncertainty for each date, as the secondary reference materials yielded dates within 1.5% of their accepted value. In total, 113 zircon grains of the 385 grains analyzed by SS-LASS yielded isochron dates < 125 Ma or at least one analysis with a ^{207}Pb-corrected ^{206}Pb/^{238}U date < 21 Ma (Table 2). Most are from three of the five samples considered (i.e. VE13-04, VE13-09, VE13-17; Table 2). Seven of the 44 zircons from VE13-09 yielded two distinct dates (Table 2). Of the 120 dates in Table 2, 37 have MSWD values slightly higher than expected for

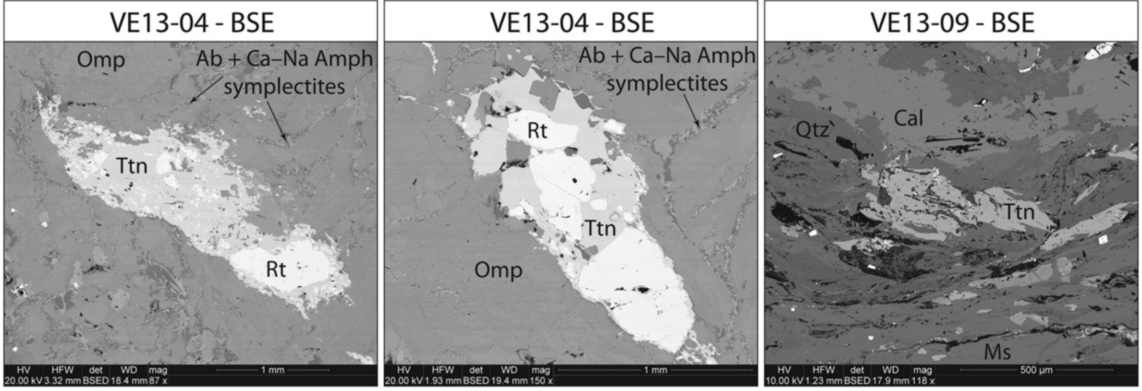

Fig. 3. BSE images of selected titanite grains from VE13-04 and VE13-09. Ab: albite, Amph: amphibole, Cal: calcite, Ms: muscovite, Omp: omphacite, Qtz: quartz, Rt: rutile, Ttn: titanite.

a single population (Wendt and Carl, 1991). These slightly high MSWD values likely reflect incomplete sampling of a second age domain within the zircon.

4.1.1. Comparison of isochron dates

The majority of the isochron/first-shot ^{207}Pb-corrected ^{206}Pb/^{238}U dates (101 of 120) lie between 40 and 10 Ma (Table 2). Probability density distribution analysis, performed for all dates in the range 40–10 Ma using the approach of Sambridge and Compston (1994), reveals discrete groupings within this range; peaks defining distinct populations occur at c. 33.2 Ma, c. 28.3 Ma, c. 23.0 Ma, and c. 18.1 Ma (Fig. 6), and generally have 2σ uncertainties of <1% (Fig. 6). The three oldest populations occur in multiple samples, and are correlated with metamorphic/zircon growth episodes at 33.0 ± 0.5 Ma, 28.3 ± 0.5 Ma and 23.0 ± 0.4 Ma (Fig. 7). These ages include uncertainties of 1.5% because the SS-LASS analysis of the reference material produced dates accurate to within 1.5% of published values. The youngest peak occurs only in VE13-09 and is associated with a zircon growth episode at 18.2 ± 0.3 Ma (Fig. 7). The probability density distribution plots for VE13-04 and VE13-09 in Fig. 6 also display a minor population at c. 42–41 Ma (Fig. 6). Despite the inclusion of 37 dates with slightly high MSWD values (likely related to incomplete sampling of a second zircon age domain), population analysis defined four distinct age groups from the SS-LASS dates of Table 2. This demonstrates robustness in the SS-LASS approach used to identify distinct zircon age populations. Complementary figures to Figs. 6 and 7, composed from the individual SS-LASS analyses (^{207}Pb-corrected ^{206}Pb/^{238}U dates) rather than the isochron dates of Table 2, are provided in the Supplementary material.

The average trace-element (Th, U, Eu, Y or Ti) abundances and Th/U ratio for each SS-LASS date from samples VE13-04, VE13-09 and VE13-

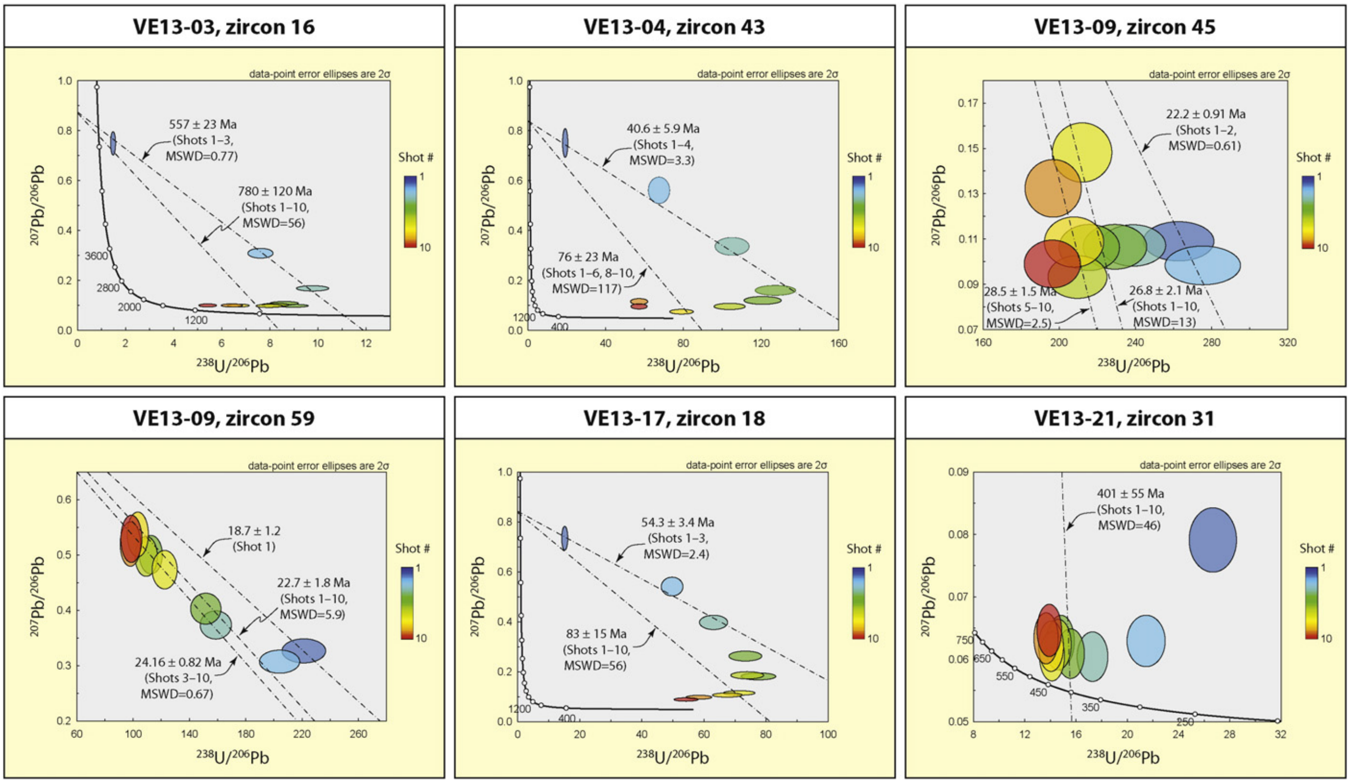

Fig. 4. Analysis populations on Tera–Wasserburg plots for selected grains from the SS-LASS work. Plots demonstrate patterns characteristic of mixing of two or more isotopic sources. Reference isochrons are anchored to common Pb of Stacey and Kramers (1975) for the age obtained. Differences between the concordia plots shown and those for the same grains in the Supplementary material relate to filtering of data for 'metamorphic' shots (filtering criteria outlined in the 'SS-LASS' sub-section of the Results).

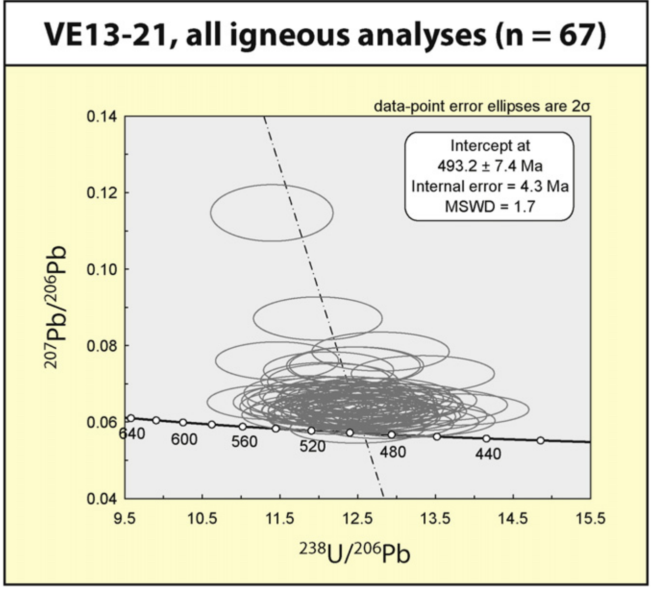

Fig. 5. Sixty-seven SS-LASS analyses made on igneous zircon of VE13-21, defining a 493.2 ± 7.4 Ma isochron. Isochron anchored to common Pb of Stacey and Kramers (1975) for the age obtained.

17 are listed in Table 2 and plotted in Fig. 8 (values and plots for individual SS-LASS analyses are given in the Supplementary material). Though there is significant scatter, some systematic trends are apparent in Fig. 8. Th, U, Eu, and Y increase with time, particularly in VE13-09; the biggest increases are between c. 28 and c. 23 Ma. Th/U is relatively constant.

4.2. Continuous-pulse LASS

A single zircon rim (as established from CL imaging) from sample VE13-04, which was large enough for analysis by continuous-pulse LASS, yielded a ^{207}Pb-corrected ^{238}U/^{206}Pb date of 33.1 ± 0.8 Ma (Fig. 2); this is equivalent to the 33.0 ± 0.5 Ma peak date in the distribution of SS-LASS analyses. A fit to all 42 titanite analyses from VE13-04 yielded a similar date of 32.6 ± 2.8 Ma (MSWD = 1.06; Fig. 9). Fifty-eight titanite analyses from VE13-09 yielded an isochron of 36.6 ± 1.1 Ma (MSWD = 1.01; Fig. 9).

Titanite from VE13-04 reveals three chemically distinct populations, as illustrated by chondrite-normalized REE patterns and groupings in Eu/Sm v. Dy/Lu space (Fig. 9). The first population, shown in blue in Fig. 9, comprises six analyses, displays a slight negative Eu anomaly (low Eu/Sm), and relatively steep slopes across the LREEs (La, Ce, Pr, Nd, Sm) and HREEs (Dy, Ho, Er, Tm, Yb, Lu; high Dy/Lu). The second population, shown in red in Fig. 9, comprises seven analyses, displays a strong positive Eu anomaly (high Eu/Sm), and relatively gentle slopes across the LREEs and HREEs (low Dy/Lu). The third population is shown in gray in Fig. 9, and displays REE patterns transitional between the blue and red populations. The data on the Tera–Wasserburg plot for VE13-04 (Fig. 9) are colored to correspond with the three compositionally distinct populations apparent in the REE plots. Isochron dates for only the blue (low Eu; 36 ± 26 Ma) and only the red (high Eu; 29.3 ± 7.6 Ma) data are also provided (Fig. 9).

5. Discussion

5.1. Igneous and metamorphic ages for the Cordillera de la Costa

The 493.2 ± 7.4 Ma U–Pb zircon SS-LASS date for the Cata orthogneiss (VE13-21; Fig. 5) is equivalent to U–Pb zircon igneous ages of other basement rocks in the Cordillera de la Costa (Choroní granite, 471 ± 23 Ma; Guaremal gneiss, 501 ± 25 Ma: Sisson et al., 2005). Sector zoning in CL (Fig. 2) and low Th/U (mostly 0.1–0.2) suggest a metamorphic or low-temperature igneous origin for zircons that yielded the 493.2 ± 7.4 Ma date. However, the presence of orthoclase augen in the Cata orthogneiss, and age correlation with the Choroní granite and Guaremal gneiss cause us to favor interpretation of the 493.2 ± 7.4 Ma date as that of the igneous protolith.

The single 33.1 ± 0.8 Ma U–Pb zircon date (Fig. 2) and 32.6 ± 2.8 Ma U–Pb titanite isochron (Fig. 9) obtained for the omphacitite (VE13-04) are identical within uncertainty and also equivalent to the main peak of the SS-LASS data (Fig. 7). These dates are taken to represent the amphibolite-facies, decompression-related overprint that is recorded in the variably retrogressed eclogite lenses of Puerto Cabello (see Morgan, 1970; Sisson et al., 1997). This interpretation rests on: i) the observation of titanite overgrowths on rutile in VE13-04 (e.g., Ernst and Liu, 1998), ii) the textural relationship between titanite and symplectic decomposition of omphacite (Fig. 3), and iii) the association of zircon overgrowths in VE13-04 with amphibolite-facies (albite + Na–Ca symplectite) healing of radial cracks in enclosing omphacite (Fig. 2). The c. 33.0 Ma SS-LASS peaks for VE13-09 and VE13-17 (Fig. 7) may also mark this amphibolite-facies metamorphism. However, despite amphibolite-facies assemblages in these rocks (see sample descriptions in Supplementary material), textures associated with zircon overgrowth are not diagnostic of their exact metamorphic context. The c. 33.0 Ma age for amphibolite-facies metamorphism at Puerto Cabello is at least 20 Myr younger than cooling ages from Isla Margarita and Villa de Cura (Table 1). This finding suggests that, despite mineralogical and petrological similarities (Morgan, 1970; Blackburn and Navarro, 1977; Maresch and Abraham, 1981; Bocchio et al., 1996; Sisson et al., 1997), the exhumation-related overprints on HP/LT assemblages at Isla Margarita and Puerto Cabello were fundamentally different in terms of timing and thus tectonic context (see Sorensen et al., 2005).

Three younger (28.3 ± 0.5 Ma, 23.0 ± 0.4 Ma, 18.2 ± 0.3 Ma) zircon overgrowth events are apparent in the U–Pb zircon SS-LASS analyses (Table 2, Fig. 7). The concentrations of Th, U, Eu and Y in zircons of VE13-04, VE13-09 and VE13-17 all increase with decreasing age between the c. 33.0, c. 28.3, c. 23.0 and c. 18.2 Ma populations (Fig. 8); this trend is most obvious for VE13-09 between the c. 28.3 and c. 23.0 Ma populations. The pattern of variation in zircon trace-element composition across the four metamorphic episodes is consistent with progressive breakdown of plagioclase and garnet between c. 33.0 and c. 18.2 Ma, and progressive breakdown of Th- and U-bearing accessory minerals and/or late introduction of fluids enriched in HFSE over the same period. The c. 23.0 and c. 18.2 Ma zircon growth events are associated with generally elevated abundances for all trace elements measured (Fig. 8), which may be indicative of significant hydrothermal zircon growth.

5.2. Significance of multiple, short-duration zircon (re)crystallization episodes

The fact that the same c. 33.0 Ma, c. 28.3 Ma and c. 23.0 Ma dates are recorded in multiple rocks (Fig. 7) is consistent with two possible scenarios: i) each of the metamorphic episodes were regional in extent and affected rocks separated by great distance and later brought together in the mélange, or ii) as Morgan (1970) and Sisson et al. (1997) contend, the mélange formed during or before HP metamorphism (prior to c. 33.0 Ma) and the metamorphic episodes (affecting the already-built mélange) may have been more local in extent. For the first scenario, repeated coordination of a simultaneous metamorphic response over great distance would require that the metamorphic episodes were related to large-scale tectonic activity. For example, the c. 33.0 Ma, c. 28.3 Ma and c. 23.0 Ma metamorphic episodes may have marked discrete tectonic events affecting the entire northern margin of South America. For the second scenario, the metamorphic

Table 2
SS-LASS isochron dates and ^{207}Pb-corrected ^{206}Pb/^{238}U dates obtained from zircon grains for which the first SS-LASS shot was <125 Ma, with trace-element abundances.

Grain	Isochron date (Ma)	MSWD	Shots used	Th (ppm)	U (ppm)	Th/U	Eu (ppm)	Y (ppm)	Ti (ppm)
VE13-03									
z5	35.3 ± 5.6	5.5	2–7	–	–	–	–	–	–
z12	8 ± 42	0.034	1–2	–	–	–	–	–	–
z51	27.3 ± 8.0	0.051	1, 5[a]	–	–	–	–	–	–
z53	31.5 ± 7.7	0.84	1–3, 9[a]	–	–	–	–	–	–
VE13-04									
z1	35.6 ± 0.8	1.6	1–9	3.3	96	0.035	–	99	1.9
z4	32.9 ± 1.4	3.0	1–10	3.6	47	0.077	–	105	1.7
z7	33.6 ± 2.1	2.2	1–8	2.6	96	0.027	–	129	1.6
z9	31.9 ± 1.4	2.7	1–9	3.6	129	0.028	–	85	1.3
z12	32.5 ± 1.2	0.71	1–4	3.7	81	0.046	–	116	2.4
z16	32.8 ± 1.5	2.5	1–8	2.6	99	0.026	–	117	1.8
z20	32.5 ± 3.1	4.3	1, 3–8[a]	1.0	87	0.012	–	52	0.80
z22	32.8 ± 1.3	2.9	1–10	3.0	106	0.029	–	81	0.60
z27	33.6 ± 1.4	3.7	1–10	2.5	100	0.025	–	207	6.1
z28	34.8 ± 1.4	2.9	1–10	3.4	30	0.11	–	185	1.6
z30	34.4 ± 1.1	0.44	2–5	3.4	187	0.018	–	114	2.3
z32	36.5 ± 1.2	1.0	2–10	2.4	245	0.0097	–	106	9.6
z33	33.8 ± 3.0	4.2	2–6	4.3	143	0.030	–	87	1.5
z35	30.8 ± 4.8	5.2	2–7	3.2	105	0.030	–	68	1.4
z41	33.4 ± 2.2	5.5	1–3, 5–10[a]	3.8	84	0.045	–	89	2.3
z43	40.6 ± 5.9	3.3	1–4	4.2	66	0.064	–	107	22
z48	33.3 ± 0.6	1.2	1–10	2.0	75	0.027	–	101	2.0
z50	32.8 ± 1.1	0.95	1–5	3.3	52	0.064	–	135	1.7
z51	30.9 ± 1.7	4.1	1–10	4.0	294	0.014	–	66	1.6
z58	34.1 ± 1.9	0.93	1–5	6.2	110	0.056	0.14	152	–
z66	31.0 ± 1.7	4.2	1–10	4.3	70	0.061	0.20	366	–
z67	29.8 ± 1.6	2.6	2–10	12	101	0.12	0.15	256	–
z69	32.1 ± 1.0	1.5	1–10	3.7	159	0.023	0.09	189	–
z70	33.0 ± 1.4	0.52	1–3	2.6	122	0.021	0.09	232	–
VE13-09									
z1	32.1 ± 1.4	1.1	1–7	8.9	157	0.057	0.38	282	–
z3	31.0 ± 3.1	4.3	1–9	11	171	0.062	0.15	220	–
z7	27.4 ± 1.7	3.1	1–2	25	1591	0.015	1.2	1075	–
z8	26.8 ± 1.2	1.6	1–2	1.2	525	0.0023	0.06	244	–
z10	30.2 ± 0.8	1.9	2–7	5.1	333	0.015	0.04	326	–
z11	23.1 ± 1.2	2.4	1–2	8.9	451	0.020	0.29	416	–
z12, older	32.3 ± 1.9	3.1	5–10	4.8	242	0.020	0.12	265	–
z12, younger	17.6 ± 1.0	0	1	160	4917	0.032	0.95	2251	–
z13	22.2 ± 1.0	2.2	1–2	16	2185	0.0075	0.44	999	–
z14	18.5 ± 1.1	0	1	28	2366	0.012	0.45	812	–
z16	28.3 ± 0.7	1.6	1–6	9.9	1111	0.0089	0.29	416	–
z17	28.4 ± 0.5	0.63	1–10	12	2773	0.0043	0.41	562	–
z18	12.8 ± 3.5	2.6	1–10	25	163	0.15	17	1142	–
z19	14.7 ± 2.3	0	1	92	593	0.15	1.2	727	–
z21	30.4 ± 4.9	4.9	1–4	28	261	0.11	0.31	338	–
z23	28.8 ± 1.2	3.6	1–10	4.3	480	0.0089	0.09	249	–
z24	21 ± 18	1.4	1–10	11	43	0.27	9.3	445	–
z25	18.8 ± 1.1	0	1	107	5854	0.018	1.6	2458	–
z27, older	27.8 ± 0.7	1.0	6–10	20	802	0.025	0.14	580	–
z27, younger	18.0 ± 1.0	0	1	309	8119	0.038	0.87	333	–
z38, older	23.7 ± 1.7	3.7	2–10	8.4	279	0.030	0.10	204	–
z38, younger	16.1 ± 1.0	0	1	56	2370	0.023	4.7	4371	–
z41	18.6 ± 1.0	0	1	338	19,661	0.017	15	5844	–
z42	22.7 ± 3.9	0.20	1–4	47	4673	0.010	0.72	1291	–
z44	22.6 ± 0.4	1.8	1–10	216	10,759	0.020	2.4	1634	–
z45, older	28.5 ± 1.5	2.5	5–10	8.2	470	0.017	0.11	365	–
z45, younger	22.2 ± 0.9	0.61	1–2	30	1349	0.022	0.29	853	–
z46	29.2 ± 0.6	1.9	1–10	2.5	638	0.0039	0.10	662	–
z47	20.1 ± 1.1	0	1	31	4711	0.0065	0.74	852	–
z49, older	23.7 ± 0.7	0.99	5–9	11	473	0.023	0.10	157	–
z49, younger	17.0 ± 1.0	0	1	100	5318	0.019	0.78	973	–
z51	26.4 ± 0.5	1.7	2–10	7.1	450	0.016	0.13	290	–
z53	25.0 ± 1.9	3.3	1–2	4.0	37	0.11	0.13	236	–
z56	19.6 ± 1.1	0	1	514	12,032	0.043	4.1	3189	–
z57	41.6 ± 1.9	1.4	1–8	40	700	0.057	0.59	421	–
z58	24.0 ± 0.7	1.8	1–8	6.4	228	0.028	0.12	150	–
z59, older	24.2 ± 0.8	0.67	3–10	10	595	0.017	0.14	413	–
z59, younger	18.7 ± 1.2	0	1	40	3110	0.013	0.54	1833	–
z61	26.6 ± 1.1	2.8	1–10	52	928	0.057	1.1	1125	–
z62, older	28.0 ± 1.5	3.4	4–10	6.8	592	0.012	0.17	343	–
z62, younger	19.1 ± 1.1	0	1	63	3307	0.019	0.65	909	–
z63	18.3 ± 1.1	0	1	92	2321	0.040	0.39	1067	–

(continued on next page)

Table 2 (*continued*)

Grain	Isochron date (Ma)	MSWD	Shots used	Th (ppm)	U (ppm)	Th/U	Eu (ppm)	Y (ppm)	Ti (ppm)
z69	18.1 ± 1.0	0	1	101	9950	0.010	1.6	1945	–
z70	22.6 ± 0.7	1.5	1–3	200	9639	0.021	2.2	3459	–
z71	17.8 ± 1.0	0	1	487	21,849	0.022	6.6	3665	–
z72	22.4 ± 1.7	3.0	1–5	25	566	0.044	0.30	896	–
z73	29.2 ± 1.9	4.6	1–10	2.2	81	0.027	0.15	288	–
z75	23.6 ± 1.3	6.4	2–10	106	2290	0.046	0.39	740	–
z76	23.2 ± 0.8	2.1	1–10	29	1611	0.018	0.27	365	–
z77	22.4 ± 1.9	4.9	1–10	8.2	72	0.11	0.16	183	–
z84	16 ± 24	0	1–2	17	85	0.20	0.18	222	–
VE13-17									
z1	55.6 ± 2.4	2.2	1–2	5.4	159	0.034	0.14	250	–
z2	27.2 ± 1.5	1.8	1–2	7.1	62	0.12	0.52	180	–
z5	30.4 ± 1.0	0.3	1–3	7.3	489	0.015	0.16	582	–
z7	26.9 ± 2.5	1.7	1–6	47	428	0.11	1.9	1103	–
z8	31.6 ± 0.9	4.3	1–6	3.5	167	0.021	0.22	263	–
z10	28.5 ± 0.7	1.5	1–10	6.6	114	0.058	0.18	287	–
z12	71.6 ± 8.4	0.053	1–2	33	105	0.31	6.0	2087	–
z14	27.9 ± 1.3	0.88	1–4	18	425	0.042	0.31	1213	–
z16	56.8 ± 1.5	0.47	1–10	8.8	203	0.043	0.27	377	–
z18	54.3 ± 3.4	2.4	1–3	27	152	0.18	0.61	770	–
z19	32.3 ± 2.5	1.5	1–10	38	104	0.36	11	3476	–
z23	35.9 ± 7.3	1.3	1–10	6.4	41	0.16	0.61	155	–
z25	44 ± 4	0.72	1–2	28	159	0.17	0.62	390	–
z29	31.9 ± 3.5	2.0	1–5	58	57	1.0	0.52	212	–
z33	26.4 ± 1.4	0.9	1–6	17	99	0.17	0.26	175	–
z34	29.9 ± 2.1	5.5	1–10	8.9	113	0.079	0.09	175	–
z37	21.8 ± 1.5	0	1	36	244	0.15	2.5	694	–
z40	20.3 ± 3.1	0	1	87	342	0.25	20	1856	–
z41	88.6 ± 2.1	1.1	1–6	28	277	0.10	0.32	336	–
z43	31.9 ± 1.6	1.3	1–2	25	123	0.20	1.0	296	–
z45	44.0 ± 7.6	1.0	1–3	44	143	0.31	0.91	489	–
z46	33.1 ± 1.5	0.85	1–5	19	113	0.17	0.60	454	–
z47	31 ± 29	7.9	1–2	23	183	0.13	0.67	393	–
z48	99.4 ± 2.1	1.3	1–7	63	707	0.089	1.2	911	–
z49	25.9 ± 4.6	0.82	1–3	20	58	0.35	0.66	174	–
z51	23.0 ± 1.2	2.0	1–2	45	196	0.23	5.7	1537	–
z52	28.4 ± 2.2	3.1	1–10	5.9	83	0.072	0.18	110	–
z53	45.2 ± 3.0	3.1	1–5	3.7	225	0.016	0.09	342	–
z66	29.2 ± 0.69	1.2	1–10	3.0	103	0.030	0.31	211	–
z68	30.8 ± 1.6	3.1	1–10	4.5	84	0.054	0.11	136	–
z70	95.9 ± 5.7	0.040	1–2	36	170	0.21	3.2	637	–
z71	34.7 ± 1.9	0.075	1–2	28	149	0.19	1.4	666	–
z75	61.3 ± 6.0	3.9	1–4	5.9	161	0.037	0.16	313	–
z79	48.3 ± 1.2	0.14	1–5	23	698	0.033	0.40	563	–
z81	75.8 ± 3.5	2.9	1–10	15	197	0.075	0.23	331	–
z84	28.3 ± 1.7	0.68	1–8	8.6	86	0.10	0.25	191	–
VE13-21									
z1	27.5 ± 9.5	0.20	1–3	–	–	–	–	–	–
z7	61 ± 25	0.19	1–3	–	–	–	–	–	–
z9	65.9 ± 3.2	1.4	1–2	–	–	–	–	–	–
z25	61.0 ± 2.8	2.6	1–2	–	–	–	–	–	–
z59	117 ± 10	1.5	1–3	–	–	–	–	–	–

[a] Intermediate shot(s) excluded from the isochron fit because the *SLaPChron* peak identification routine failed to recognize peak(s) for one or all of ^{206}Pb, ^{207}Pb and ^{238}U (i.e. no ^{207}Pb/^{206}Pb and/or ^{238}Pb/^{206}Pb values were obtained) for the shot(s).

episodes may represent: i) punctuated thermodynamic response (internal self-organization within and across lithologies) to a single, protracted (c. 33–22 Ma) tectonothermal process, or ii) coordinated response to multiple and discrete, local-to-regional-scale tectonothermal events.

Fig. 10 provides a summary of the SS-LASS dates of Table 2 and comparison with published geo-/thermochronology from the Cordillera de la Costa. There are only 14 K–Ar/Ar–Ar dates for the Cordillera de la Costa (Table 1), but 11 of these were obtained from mica schists, gneisses and garnet amphibolites in and surrounding the mélange at Puerto Cabello (Table 1), from which the SS-LASS samples were also obtained. The K–Ar/Ar–Ar dates may correlate with the populations recognized in the zircon LASS data. Of the most-precise K–Ar/Ar–Ar dates, three in the range 34.2–32.9 Ma overlap the 33.0 ± 0.5 Ma SS-LASS population, and one 28.0 Ma date corresponds to the 28.3 ± 0.5 Ma SS-LASS population (Fig. 10). Two older, 42.6 Ma and 42.3 Ma dates match small peaks at 42–41 Ma in the probability density distribution plots for VE13-04 and VE13-09 (Figs. 6, 10).

Apatite and zircon fission-track dates for basement gneisses and granites of the Cordillera de la Costa (Kohn et al., 1984; Sisson et al., 2005) fall in two clusters, 24–23 Ma and 20–14 Ma (Table 1; Fig. 10). The older cluster is equivalent to the 23.0 ± 0.4 Ma population in the SS-LASS data and the younger overlaps the 18.2 ± 0.3 Ma population (Fig. 10). For zircon to grow at the low temperatures recorded by the fission-track ages, the late zircon overgrowths would have to be hydrothermal in origin. This hydrothermal activity would have to have been coeval with episodes of rapid uplift (cooling) of the basement units of the Cordillera de la Costa.

There is a coincidence in all four types of date—U–Pb zircon, U–Pb titanite, K–Ar/Ar–Ar mica or amphibole, and apatite or zircon fission track (Fig. 10)—suggesting that the c. 33.0, c. 28.3, c. 23.0 and c.

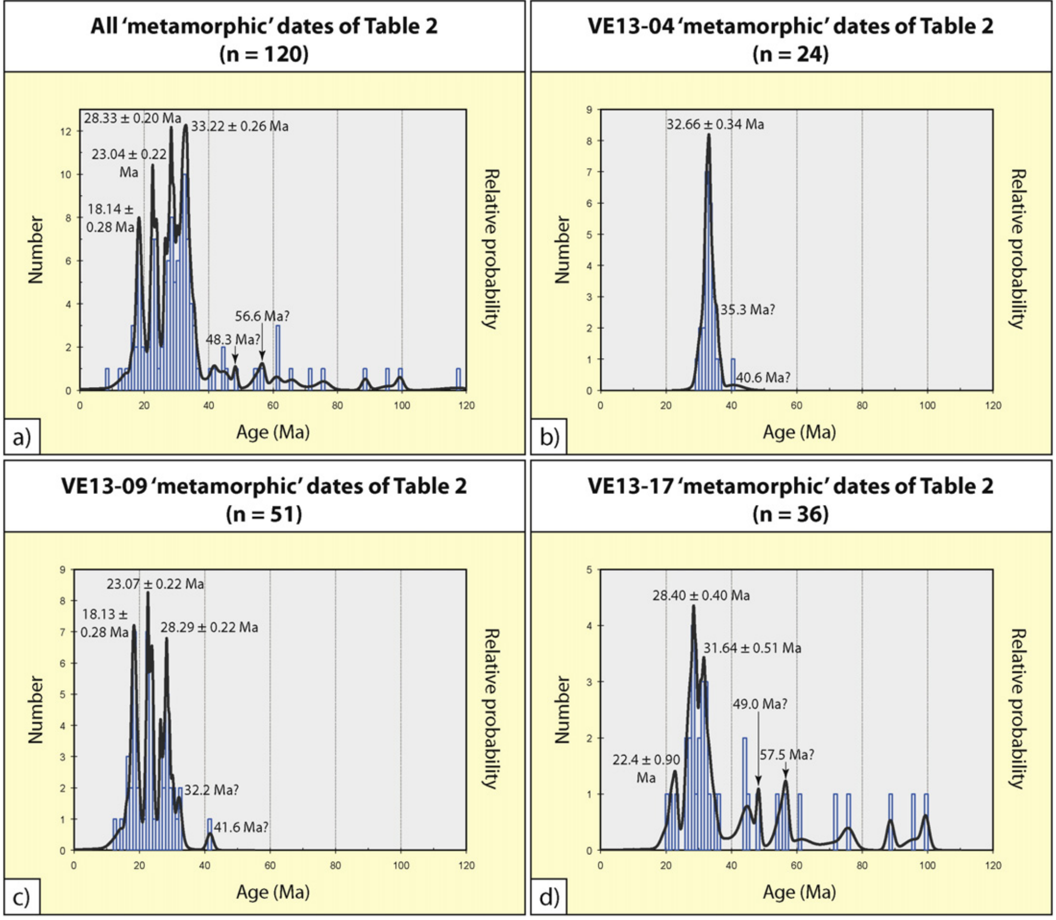

Fig. 6. Probability density distribution diagram for SS-LASS dates of Table 2. Plots show probability density distributions for: a) all analyses; b) analyses only from omphacitite VE13-04; c) analyses only from graphitic mica calc-schist VE13-09, and d) analyses only from graphitic mica schist VE13-17. Bins for histograms are 1 Ma wide.

18.2 Ma populations in the SS-LASS data signify separate geologic 'events' separated by hiatuses. This coincidence may mean that zircon overgrowths occurred during short-duration thermal and/or fluid pulses that also reset K–Ar/Ar–Ar and/or fission-track dates. For short-duration (hydro)thermal pulses, closure ages essentially record metamorphism, meaning that the K–Ar/Ar–Ar and fission-track dates are geochronological rather than thermochronological dates. Coincidence between SS-LASS dates of short-timescale metamorphism and the published K–Ar/Ar–Ar and fission-track dates leads us to the following interpretations for the origin of the zircon LASS populations:

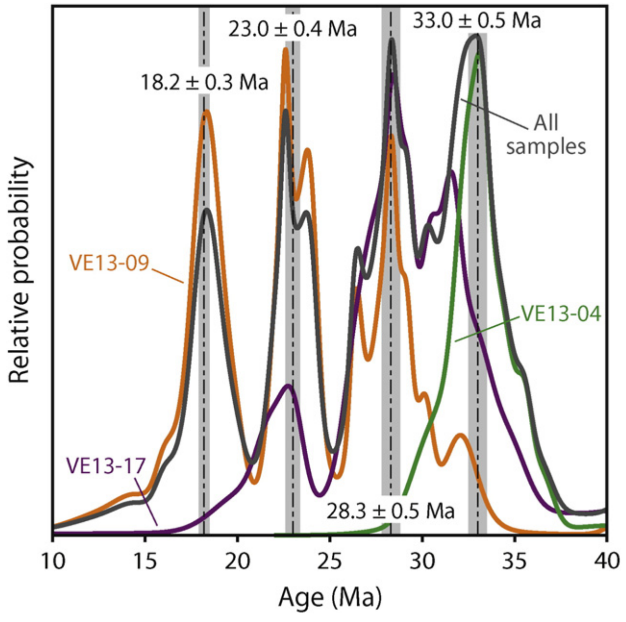

Fig. 7. Summary probability density curves for SS-LASS dates from Table 2. Shaded bands represent distinct age peaks.

i) the c. 33.0 Ma and c. 28.3 Ma populations date episodes of amphibolite-facies metamorphism driven by brief and distinct episodes of regional tectonothermal activity (e.g. thermal advection and/or localized mechanical heating associated with tectonism);
ii) the c. 23.0 Ma and c. 18.2 Ma populations date distinct episodes of enhanced fluid activity related to brief episodes of regional tectonic activity involving rapid basement uplift, and
iii) self-organized bursts of metamorphic mineral growth played only a secondary role in producing the multiple, short-duration episodes of metamorphism.

Although the various units of the Puerto Cabello mélange most likely experienced a common P–T history, not all metamorphic episodes were recorded in all rocks. This may relate to the availability of fluids and/or response of different bulk-rock compositions to the different metamorphic episodes, underlining the advantage gained by using large geochronology datasets to reconstruct the tectonothermal history of a region.

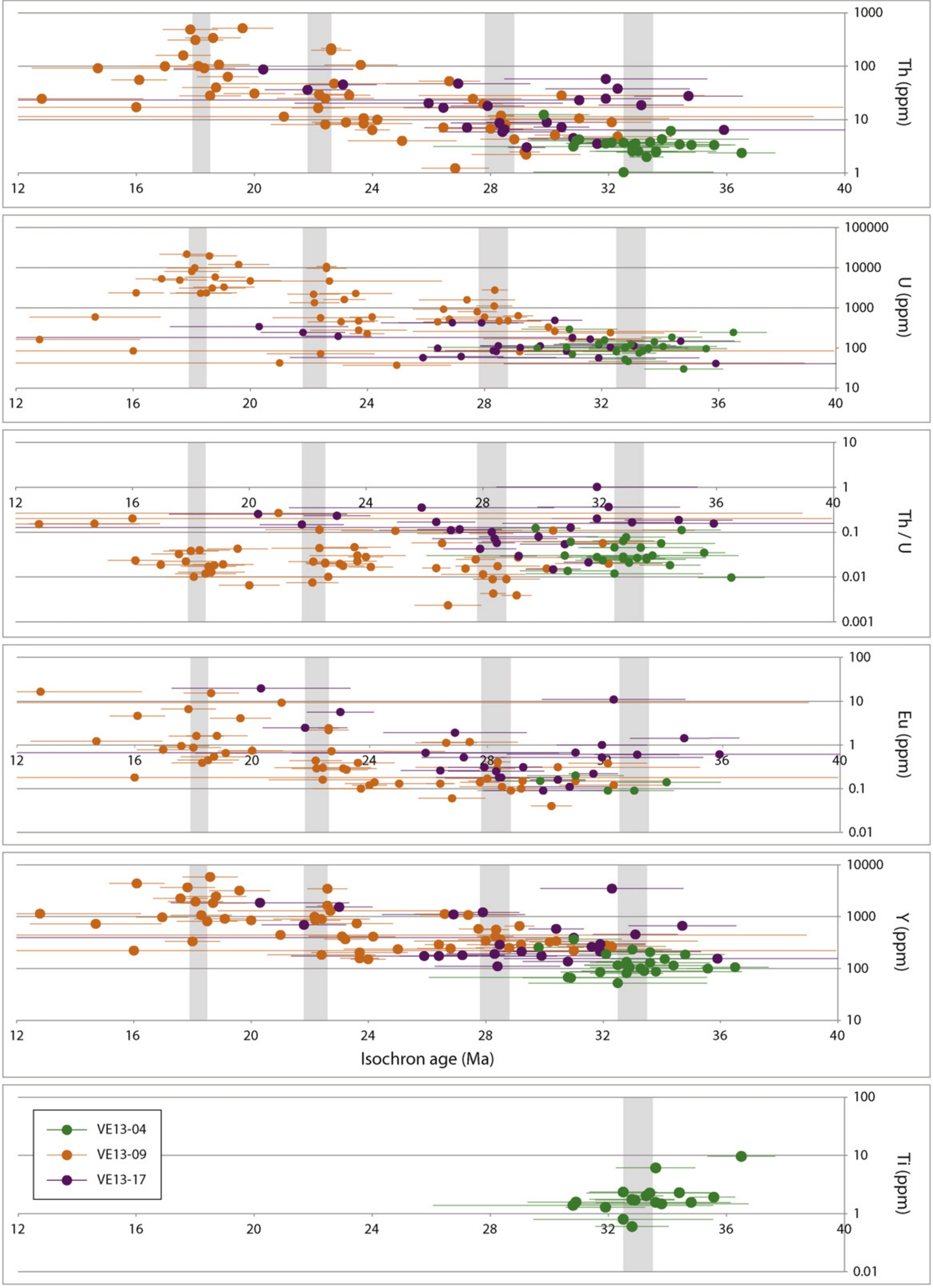

Fig. 8. Trace-element composition (Th, U, Eu, Y, Ti) and Th/U for SS-LASS dates from Table 2. Shaded regions indicate date populations of Fig. 7. Vertical axes are logarithmic. Key for Ti plot applicable to all plots. Data point size includes a ~20% uncertainty in elemental abundance or ratio.

5.3. SS-LASS v. continuous-pulse LASS for recognition of multiple, short-duration metamorphic events

As discussed above, continuous-pulse LASS yielded 33.1 ± 0.8 Ma U–Pb zircon (Fig. 2) and 32.6 ± 2.8 Ma U–Pb titanite (Fig. 9) dates. These dates are associated with thin-section textures relating zircon rim and titanite growth to amphibolite-facies overprint of the higher-pressure assemblages in VE13-04. For VE13-04, it would appear that conventional, continuous-pulse LASS was able to discern the exact timing and nature of the amphibolite-facies metamorphism. The chondrite-

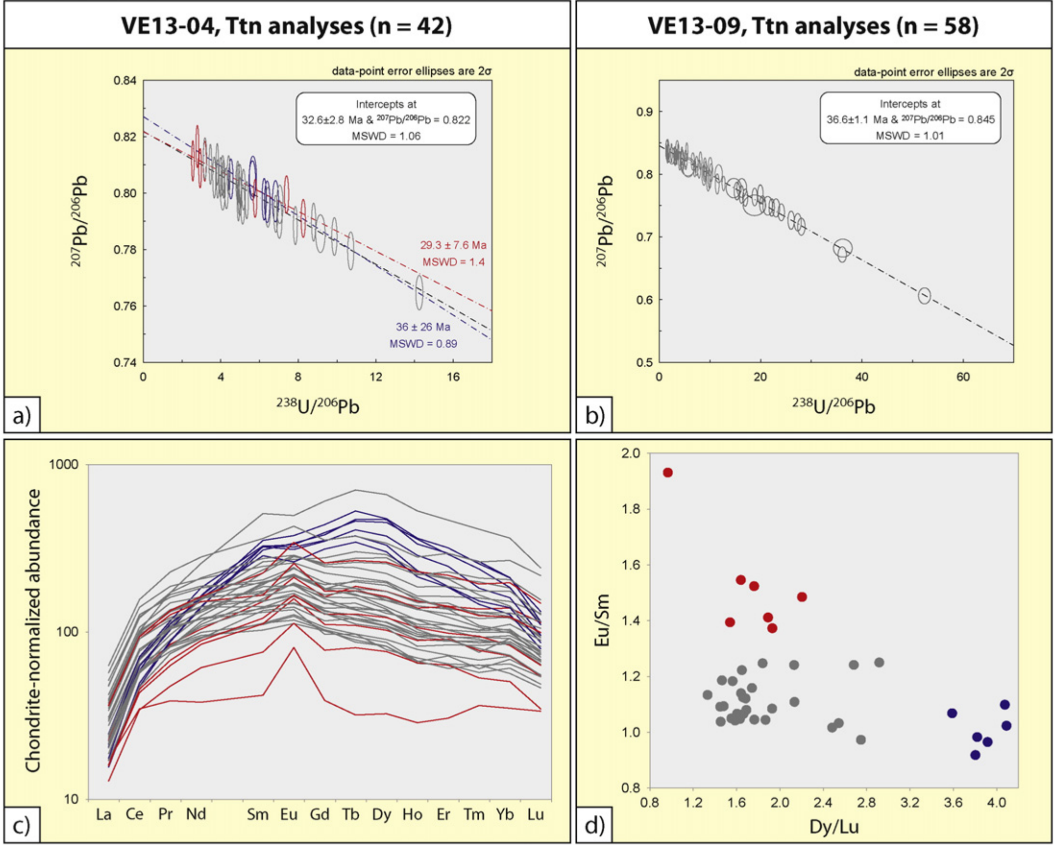

Fig. 9. Tera–Wasserburg plots for titanite analyses from: a) VE13-04, and b) VE13-09, showing best-fit isochrons for all data (black, broken lines; date and ^{207}Pb/^{206}Pb intercept in white box). Isochron dates for the red and blue data of VE13-04 are also provided. Trace element data for VE13-04 include: c) chondrite-normalized REE abundance plot (vertical axis logarithmic), and d) Eu/Sm v. Dy/Lu discrimination diagram. Blue, gray and red data for VE13-04 in c) and d) correspond to similarly colored data in a).

normalized REE plots for VE13-04 (Fig. 9), however, show that at least two (and possibly three) compositionally distinct populations of titanite contributed to the 32.6 ± 2.8 Ma U–Pb titanite date. Did the trace-element supply in VE13-04 vary significantly during a single, short period of titanite growth at c. 32.6 Ma, or were the continuous-pulse LASS analyses that produced the 32.6 ± 2.8 Ma U–Pb titanite date unable to

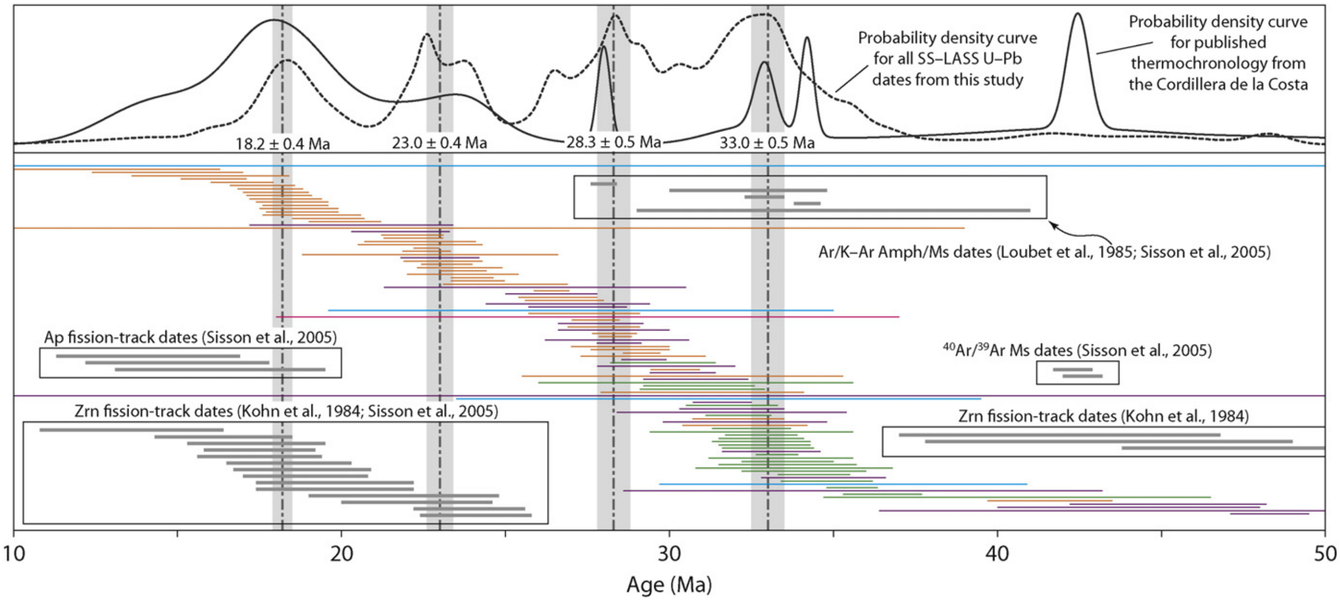

Fig. 10. Summary diagram for geochronology of the Cordillera de la Costa. Colored data are SS-LASS isochron dates from Table 2. Quartzite VE13-03 in cyan, omphacitite VE13-04 in green, graphitic mica calc-schist VE13-09 in orange, graphitic mica schist VE13-17 in purple, orthogneiss VE13-21 in pink. Gray data are published thermochronology from Table 1 (excluding typically unreliable K–Ar/Ar–Ar Bt dates). Shaded bands correspond to distinct age peaks in the SS-LASS data. Probability density curves at top represent SS-LASS dates and published thermochronology of the Cordillera de la Costa. Amph: amphibole, Ap: apatite, Bt: biotite, Ms: muscovite, Zrn: zircon.

resolve mixtures of analyte belonging to two or more distinct titanite growth (metamorphic) events? The U–Pb zircon SS-LASS data suggest an answer.

The c. 33.0 Ma zircon growth event in the SS-LASS data is associated with lower Eu, Th, U, and Y abundances than the c. 28.3 Ma zircon growth event (Fig. 8). Yttrium behaves like a HREE. Thus, the negative Eu anomalies (low Eu/Sm) and relatively steep slopes across the HREEs (high Dy/Lu) for the blue data from VE13-04 (Fig. 9) are consistent with relatively low Eu and Y abundances. Conversely, positive Eu anomalies (high Eu/Sm) and relatively gentle slopes across the HREEs (low Dy/Lu) for the red data (Fig. 9) are consistent with relatively high Eu and Y abundances. The blue and red data for titanite in Fig. 9 may correspond to the c. 33.0 and c. 28.3 Ma populations from the SS-LASS data, respectively.

When considered separately, the blue data of Fig. 9 yield an isochron date of 36 ± 26 Ma and the red data yield an isochron date of 29.3 ± 7.6 Ma. The gray data of Fig. 9 may represent sampling of mixed older (blue; c. 33.0 Ma) and younger (red; c. 28.3 Ma) titanite populations. SS-LASS may be capable of resolving individual, short-duration metamorphic growth events that, perhaps due to larger sampling volumes and smaller population statistics, the continuous-pulse LASS approach cannot.

In summary, SS-LASS yields similar uncertainties to conventional geochronology approaches, but samples far smaller zircon volumes and requires significantly less analysis time. This enables SS-LASS to amass large, multimodal datasets for zircons with multiple generations of submicron-thick metamorphic overgrowths. Combined with an accuracy of <1.5%, these advantages provide SS-LASS with unique potential for testing claims of brief (<10^6 yr) and episodic metamorphism in rocks that are Cenozoic or younger in age.

6. Conclusions

Using an added uncertainty of 5% on secondary reference materials and unknowns, SS-LASS analyses yielded single age populations; those ages are accurate to <1.5% in reference materials, suggesting a similar confidence in the unknown age populations. Such uncertainties could conceivably allow time scale resolutions of <10^6 yr for Paleogene rocks and <350 kyr for Neogene rocks.

When applied to five metamorphic rocks from the Cordillera de la Costa, Venezuela the SS-LASS technique was able to decipher multiple episodes of zircon overgrowths. These zircon growth events were correlated to regionally significant, short-duration (<10^6 yr) episodes of (hydro)thermal activity at c. 33.0, c. 28.3, c. 23.0 and c. 18.2 Ma. Given that the majority of the zircons grew metamorphic rims <1 μm thick—which cannot be dated by conventional geochronology techniques—SS-LASS provides tremendous promise for work aimed at probing the veracity of short-duration metamorphic time scales (10^4–10^6 yr) obtained from diffusion modeling (geospeedometry) approaches.

Acknowledgments

Herwart Viete provided assistance in the field in Venezuela and helped shape ideas during discussions on the geology of northern Venezuela. Joel Alvarez Landa provided local knowledge of outcrop localities and accessibility. Mike Stearns and John Cottle provided invaluable assistance with processing of the SS-LASS data. Gareth Seward helped with imaging of samples on the SEM. A 12-month Fulbright Victoria Fellowship awarded to DRV by the Australian–American Fulbright Commission enabled the study. DRV also acknowledges an International Junior Research Fellowship cofunded by Durham University and Marie Curie Actions of the European Union. Field and analytical costs were covered by UCSB.

Appendix A. Supplementary data

Supplementary data to this article can be found online at http://dx.doi.org/10.1016/j.chemgeo.2015.09.013.

References

Abbott, S.S., Harrison, T.M., Schmitt, A.K., Mojzsis, S.J., 2012. A search for thermal excursions from ancient extraterrestrial impacts using Hadean zircon Ti–U/Th–Pb profiles. Proc. Natl. Acad. Sci. 109, 13486–13492.

Ague, J.J., Baxter, E.F., 2007. Brief thermal pulses during mountain building recorded by Sr diffusion in apatite and multicomponent diffusion in garnet. Earth Planet. Sci. Lett. 261, 500–516.

Aleinikoff, J.N., Wintsch, R.P., Tolloh, R.P., Unruh, D.M., Fanning, C.M., Schmitz, M.D., 2007. Ages and origins of rocks of the Killingworth Dome, south-central Connecticut: implications for tectonic evolution of southern New England. Am. J. Sci. 307, 63–118.

Amelin, Y., Zaitsev, A.N., 2002. Precise geochronology of phoscorites and carbonatites: The critical role of U-series disequilibrium in age interpretations. Geochim. Cosmochim. Acta 66, 2399–2419.

Audemard, F.A., Cox, J.W., Dart, R.L., Machette, M.N., 2000. Map of Quaternary Faults of Venezuela: Open File Report 00-018. USGS, FUNVISIS, INTEVEP, PDVSA.

Avé Lallemant, H.G., 1997. Transpression, displacement partitioning, and exhumation in the eastern Caribbean/South American plate boundary zone. Tectonics 16, 272–289.

Avé Lallemant, H.G., Sisson, V.B., 2005. Exhumation of eclogites and blueschists in northern Venezuela: constraints from kinematic analysis of deformed structures. In: Avé Lallemant, H.G., Sisson, V.B. (Eds.), Caribbean–South American Plate InteractionsGeological society of America special papers 394. Geological Society of America, Boulder, pp. 193–206.

Baldwin, S.L., Monteleone, B.D., Webb, L.E., Fitzgerald, P.G., Grove, M., Hill, E.J., 2004. Pliocene eclogite exhumation at plate tectonic rates in eastern Papua New Guinea. Nature 431, 263–267.

Baxter, E.F., Ague, J.J., DePaolo, D.J., 2002. Prograde temperature-time evolution in the Barrovian type-locality constrained by Sm/Nd garnet ages from Glen Clova, Scotland. J. Geol. Soc. 159, 71–82.

Bellizia, A., Dengo, G., 1990. The Caribbean Mountain system, northern South America; a summary. In: Dengo, G., Case, J.E. (Eds.), The Caribbean Region. Geological Society of America, Boulder, pp. 167–175.

Belousova, E.A., Griffin, W.L., O'Reilly, S.Y., Fisher, N.I., 2002. Igneous zircon: trace element composition as an indicator of source rock type. Contrib. Mineral. Petrol. 143, 602–622.

Blackburn, W.H., Navarro, E., 1977. Garnet zoning and polymetamorphism in eclogitic rocks of Isla de Margarita, Venezuela. Can. Mineral. 15, 257–266.

Bocchio, R., De Capitani, L., Liborio, G., Maresch, W.V., Mottana, A., 1996. Equilibration conditions of eclogite lenses from Isla Margarita, Venezuela: Implication for the tectonic evolution of the metasedimentary Juan Griego Group. Lithos 37, 39–59.

Breeding, C.M., Ague, J.J., Grove, M., Rupke, A.I., 2004. Isotopic and chemical alteration of zircon by metamorphic fluids: U–Pb depth profiling of zircon crystals from Barrow's garnet zone, northeast Scotland. Am. Mineral. 89, 1067–1077.

Camacho, A., Lee, J.K.W., Hensen, B.J., Braun, J., 2005. Short-lived orogenic cycles and the eclogitization of cold crust by spasmodic hot fluids. Nature 435, 1191–1196.

Carson, S.S., Ague, J.J., Grove, M., Coath, C.D., Harrison, T.M., 2002. U–Pb isotopic behaviour of zircon during upper-amphibolite facies fluid infiltration in the Napier Complex, east Antarctica. Earth Planet. Sci. Lett. 199, 287–301.

Chamberlain, K.J., Wilson, C.J.N., Wooden, J.L., Charlier, B.L.A., Ireland, T.R., 2014. New perspectives on the Bishop Tuff from zircon textures, ages and trace elements. J. Petrol. 55, 395–426.

Chen, R.-X., Zheng, Y.-F., Xie, L., 2010. Metamorphic growth and recrystallization of zircon: distinction by simultaneous in situ analyses of trace elements, U/Th/Pb and Lu/Hf isotopes in zircons from eclogite facies rocks in the Sulu orogen. Lithos 114, 132–154.

Chen, R.-X., Ding, B., Zheng, Y.-F., Hu, Z., 2015. Multiple episodes of anatexis in a collisional orogen: zircon evidence from migmatite in the Dabie orogen. Lithos 212–215, 247–265.

Cherniak, D.J., Watson, E.B., 2003. Diffusion in zircon. Rev. Mineral. Geochem. 53, 113–144.

Cherniak, D.J., Watson, E.B., Grove, M., Harrison, T.M., 2004. Pb diffusion in monazite: a combined RBS/SIMS study. Geochim. Cosmochim. Acta 68, 829–840.

Christensen, J.N., Rosenfeld, J.L., DePaolo, D.J., 1989. Rates of tectonometamorphic processes from rubidium and strontium isotopes in garnet. Science 244, 1465–1469.

Christensen, J.N., Selverstone, J., Rosenfeld, J.L., DePaolo, D.J., 1994. Correlation by Rb–Sr geochronology of garnet growth histories from different structural levels within the Tauern Window, Eastern Alps. Contrib. Mineral. Petrol. 118, 1–12.

Cottle, J.M., Horstwood, M.S.A., Parrish, R.R., 2009. A new approach to single shot laser ablation analysis and its application to *in situ* Pb/U geochronology. J. Anal. At. Spectrom. 24, 1355–1363.

Cottle, J.M., Kylander-Clark, A.R., Vrijmoed, J.C., 2012. U–Th/Pb geochronology of detrital zircon and monazite by single shot laser ablation inductively coupled plasma mass spectrometry (SS-LA-ICPMS). Chem. Geol. 332–333, 136–147.

Donaldson, D.G., Webb, A.A.G., Menold, C.A., Kylander-Clark, A.R.C., Hacker, B.R., 2013. Petrochronology of Himalayan ultrahigh-pressure eclogite. Geology 41, 835–838.

Dragovic, B., Samanta, L.M., Baxter, E.F., Selverstone, J., 2012. Using garnet to constrain the duration and rate of water-releasing metamorphic reactions during subduction: an example from Sifnos, Greece. Chem. Geol. 314–317, 9–22.

Ducea, M.N., Ganguly, J., Rosenberg, E.J., Patchett, P.J., Cheng, W., Isachsen, C., 2003. Sm–Nd dating of spatially controlled domains of single crystals: a new method of high-temperature thermochronology. Earth Planet. Sci. Lett. 213, 31–42.

Eggins, S.M., Rudnick, R.L., McDonough, W.F., 1998. The composition of peridotites and their minerals: a laser-ablation ICP–MS study. Earth Planet. Sci. Lett. 154, 53–71.

Eggins, S.M., Grün, R., McCulloch, M.T., Pike, A.W.G., Chappell, J., Kinsley, L., Mortimer, G., Shelley, M., Murray-Wallace, C.V., Spötl, C., Taylor, L., 2005. In situ U-series dating by laser ablation multi-collector ICP-MS: new prospects for Quaternary geology. Quat. Sci. Rev. 24, 2523–2538.

Ernst, W.G., Liu, J., 1998. Experimental phase-equilibrium study of Al- and Ti-contents of calcic amphibole in MORB — a semiquantitative termobarometer. Am. Mineral. 83, 952–969.

Faryard, S.W., Chakraborty, S., 2005. Duration of Eo-Alpine metamorphic events obtained from multicomponent diffusion modeling of garnet: a case study from the Eastern Alps. Contrib. Mineral. Petrol. 150, 306–318.

Foster, G., Kinny, P., Vance, D., Prince, C., Harris, N., 2000. The significance of monazite U/Th–Pb age data in metamorphic assemblages; a combined study of monazite and garnet chronometry. Earth Planet. Sci. Lett. 181, 327–340.

Foster, G., Gibson, H.D., Parrish, R., Horstwood, M., Fraser, J., Tindle, A., 2002. Textural, chemical and isotopic insights into the nature and behaviour of metamorphic monazite. Chem. Geol. 191, 182–207.

Gasser, D., Rubatto, D., Bruand, E., Stüwe, K., 2012. Large-scale short-lived metamorphism, deformation and magmatism in the Chugach metamorphic complex, southern Alaska: a SHRIMP U–Pb study of zircons. Geol. Soc. Am. Bull. 124, 886–905.

Giunta, G., Beccaluva, L., Coltorti, M., Siena, F., Vaccaro, C., 2002. The southern margin of the Caribbean Plate in Venezuela: tectono-magmatic setting of the ophiolitic units and kinematic evolution. Lithos 63, 19–40.

Grove, M., Harrison, T.M., 1999. Monazite Th–Pb age depth profiling. Geology 27, 487–490.

Hermann, J., Rubatto, D., 2003. Relating zircon and monazite domains to garnet growth zones: age and duration of granulite facies metamorphism in the Val Malenco lower crust. J. Metamorph. Geol. 21, 833–852.

Herwartz, D., Nagel, T.J., Münker, C., Scherer, E.E., Froitzheim, N., 2011. Tracing two orogenic cycles in one eclogite sample by Lu–Hf garnet chronometry. Nat. Geosci. 4, 178–183.

Hoskin, P.W.O., Ireland, T.R., 2000. Rare earth element chemistry of zircon and its use as a provenance indicator. Geology 28, 627–630.

Hoskin, P.W.O., Schaltegger, U., 2003. The composition of zircon and igneous and metamorphic petrogenesis. Rev. Mineral. Geochem. 53, 27–62.

Jackson, S.E., Pearson, N.J., Griffin, W.L., Belousova, E.A., 2004. The application of laser ablation-inductively coupled plasma-mass spectrometry to in situ U/Pb zircon geochronology. Chem. Geol. 211, 47–69.

Jaffey, A.H., Flynn, K.F., Glendenin, L.E., Bentley, W.C., Essling, A.M., 1971. Precision measurement of the half-lives and specific activities of ^{235}U and ^{238}U. Phys. Rev. C 4, 1889–1906.

Johnston, S., Hacker, B.R., Ducea, M.N., 2007. Exhumation of ultrahigh-pressure rocks beneath the Hornelen segment of the Nordfjord-Sogn Detachment Zone, western Norway. Geol. Soc. Am. Bull. 119, 1232–1248.

Johnston, S., Gehrels, G., Valencia, V., Ruiz, J., 2009. Small-volume U–Pb zircon geochronology by laser ablation-multicollector-ICP-MS. Chem. Geol. 259, 218–229.

Kelly, C.J., McFarlane, C.R.M., Schneider, D.A., Jackson, S.E., 2014. Dating micrometre-thin rims using a LA-ICP-MS depth-profiling technique on zircon from an Archaean metasediment: comparison with the SIMS depth-profiling method. Geostand. Geoanal. Res. 38, 389–407.

Kohn, B.P., Shagam, R., Subieta, T., 1984. Results and preliminary implications of sixteen fission-track ages from rocks of the western Caribbean Mountains, Venezuela. In: Bonini, W.E., Hargraves, R.B., Shagham, R. (Eds.), The Caribbean–South American Boundary and Regional TectonicsGeological Society of America Memoirs 162. Geological Society of America, Boulder, pp. 415–422.

Kohn, M.J., 2009. Models for garnet differential geochronology. Geochim. Cosmochim. Acta 73, 170–182.

Kohn, M.J., Corrie, S.L., 2011. Preserved Zr-temperatures and U–Pb ages in high-grade metamorphic titanite: evidence for a static hot channel in the Himalayan orogen. Earth Planet. Sci. Lett. 311, 136–143.

Kohn, M.J., Wieland, M.S., Parkinson, C.D., Upreti, B.N., 2005. Five generations of monazite in Langtang gneisses: implications for formation of the Himalayan metamorphic core. J. Metamorph. Geol. 23, 300–406.

Kylander-Clark, A.R.C., Hacker, B.R., Johnson, C.M., Beard, B.L., Mahlen, N.J., Lapen, T.J., 2007. Coupled Lu–Hf and Sm–Nd geochronology constrains prograde and exhumation histories of high- and ultrahigh-pressure eclogites from western Norway. Chem. Geol. 242, 137–154.

Kylander-Clark, A.R.C., Hacker, B.R., Mattinson, J.M., 2008. Slow exhumation of UHP terranes: titanite and rutile ages of the Western Gneiss Region, Norway. Earth Planet. Sci. Lett. 272, 531–540.

Kylander-Clark, A.R.C., Hacker, B.R., Cottle, J.M., 2013. Laser ablation split-stream ICP petrochronology. Chem. Geol. 345, 99–112.

Lagos, M., Scherer, E.E., Tomaschek, F., Münker, C., Keiter, M., Berndt, J., Ballhaus, C., 2007. High precision Lu–Hf geochronology of Eocene eclogite-facies rocks from Syros, Cyclades, Greece. Chem. Geol. 243, 16–35.

Lancaster, P.J., Baxter, E.F., Ague, J.J., Breeding, C.M., Owens, T.L., 2008. Synchronous peak Barrovian metamorphism driven by syn-orogenic magmatism and fluid flow in southern Connecticut, USA. J. Metamorph. Geol. 26, 527–538.

Lapen, T.J., Johnson, C.M., Baumgartner, L.P., Mahlen, N.J., Beard, B.L., Amato, J.M., 2003. Burial rates during prograde metamorphism of an ultra-high-pressure terrane: an example from Lago di Cignana, western Alps, Italy. Earth Planet. Sci. Lett. 215, 57–72.

Lister, G.S., Forster, M.A., Rawling, T.J., 2001. Episodicity during orogenesis. In: James, K.H., Lorente, M.A., Pindell, J.L. (Eds.), Continental Reactivation and ReworkingGeological Society of London Special Publications 184. The Geological Society, London, pp. 89–113.

Liu, Y.S., Hu, Z.C., Zong, K.Q., Gao, C.G., Gao, S., Xu, J., Chen, H.H., 2010. Reappraisement and refinement of zircon U–Pb isotope and trace element analyses by LA-ICP-MS. Chin. Sci. Bull. 55, 1535–1546.

Loubet, M., Montigny, R., Chachati, B., Duarte, N., Lambret, B., Martin, C., Thuizat, R., 1985. Geochemical and geochronological constraints on the geodynamic development of the Caribbean Chain of Venezuela. In: Alain, M. (Ed.), Symposium Géodynamique des Caraibes, Paris, 5–8 Février 1985.

Maresch, W.V., Abraham, K., 1981. Petrology, mineralogy and metamorphic evolution of an eclogite from the Island of Margarita, Venezuela. J. Petrol. 22, 333–362.

Maresch, W.V., Kluge, F., Baumann, A., Pindell, J.L., Krückhans-Lueder, G., Stanek, K.-P., 2009. The occurrence and timing of high-pressure metamorphism on Margarita Island, Venezuela: a constraint on Caribbean–South American interaction. In: James, K.H., Lorente, M.A., Pindell, J.L. (Eds.), The Origin and Evolution of the Caribbean PlateGeological society of london special publications 328. The Geological Society, London, pp. 705–741.

Menéndez, A., 1966. Tectónica de la parte central de las Montañas Occidentales del Caribe, Venezuela. Bol. Geol. (Caracas) 8, 116–139.

Mojzsis, S.J., Harrison, T.M., 2002. Establishment of a 3.83-Ga magmatic age for the Akilia tonalite (southern West Greenland). Earth Planet. Sci. Lett. 202, 563–576.

Morgan, B.A., 1970. Petrology and mineralogy of eclogite and garnet amphibolite from Puerto Cabello, Venezuela. J. Petrol. 11, 101–145.

Oliver, G.J.H., Chen, F., Buchwaldt, R., Hegner, E., 2000. Fast tectonometamorphism and exhumation in the type area of the Barrovian and Buchan zones. Geology 28, 459–462.

Ostos, M., Sisson, V.B., 2005. Geochemistry and tectonic setting of igneous and metaigneous rocks of northern Venezuela. In: Avé Lallemant, H.G., Sisson, V.B. (Eds.), Caribbean–South American Plate InteractionsGeological Society of America Special Papers 394. Geological Society of America, Boulder, pp. 119–156.

Ostos, M., Yoris, F., Avé Lallemant, H.G., 2005. Overview of the southeast Caribbean–South American plate boundary zone. In: Avé Lallemant, H.G., Sisson, V.B. (Eds.), Caribbean–South American Plate InteractionsGeological Society of America Special Papers 394. Geological Society of America, Boulder, pp. 53–89.

Paton, C., Woodhead, J.D., Hellstrom, J.C., Hergt, J.M., Greig, A., Maas, R., 2010. Improved laser ablation U–Pb zircon geochronology through robust downhole fractionation correction. Geochem. Geophys. Geosyst. 11. http://dx.doi.org/10.1029/2009GC002618.

Pearce, N.J.G., Perkins, W.T., Westgate, J.A., Gorton, M.P., Jackson, S.E., Neal, C.R., Chenery, S.P., 1997. A compilation of new and published major and trace element data for NIST SRM 610 and NIST SRM 612 glass reference materials. Geostand. Geoanal. Res. 21, 115–144.

Perchuk, A., Philippot, P., 1997. Rapid cooling and exhumation of eclogitic rocks from the Great Caucasus, Russia. J. Metamorph. Geol. 15, 299–310.

Pindell, J., Kennan, L., Stanek, K.-P., Maresch, W.V., Draper, G., Higgs, R., 2005. Plate-kinematics and crustal dynamics of circum-Caribbean arc-continent interactions: tectonic controls on basin development in proto-Caribbean margins. In: Avé Lallemant, H.G., Sisson, V.B. (Eds.), Caribbean–South American Plate InteractionsGeological society of America special papers 394. Geological Society of America, Boulder, pp. 7–52.

Pindell, J., Kennan, L., Stanek, K.-P., Maresch, W.V., Draper, G., 2006. Foundations o Mexico and Caribbean evolution: eight controversies resolved. Geol. Acta 4, 303–341.

Plotnikov, A., Vogt, C., Hoffmann, V., Täschner, C., Wetzig, K., 2001. Application of laser ablation inductively coupled quadrupole plasma mass spectrometry (LA-ICP-QMS) for depth profile analysis. J. Anal. At. Spectrom. 16, 1290–1295.

Pollington, A.D., Baxter, E.F., 2010. High resolution Sm–Nd garnet geochronology reveals the uneven pace of tectonometamorphic processes. Earth Planet. Sci. Lett. 153, 1–28.

Pollington, A.D., Baxter, E.F., 2011. High precision microsampling and preparation of zoned garnet porphyroblasts for Sm–Nd geochronology. Chem. Geol. 281, 270–282.

Pullen, A., Ibañez-Mejía, M., Gehrels, G.E., Ibañez-Mejía, J.C., Pecha, M., 2014. What happens when $n = 1000$? Creating large-n geochronological datasets with LA-ICP-MS for geologic investigations. J. Anal. At. Spectrom. 29, 971–980.

Raimbourg, H., Goffé, B., Jolivet, L., 2007. Garnet reequilibration and growth in the eclogite facies and geodynamical evolution near peak metamorphic conditions. Contrib. Mineral. Petrol. 153, 1–28.

Romer, R.L., 2003. Alpha recoil in U–Pb geochronology: effective sample size matters. Contrib. Mineral. Petrol. 145, 481–491.

Rubatto, D., 2002. Zircon trace element geochemistry: partitioning with garnet and the link between U–Pb ages and metamorphism. Chem. Geol. 184, 123–138.

Rubatto, D., Gebauer, D., Compagnoni, R., 1999. Dating of eclogite-facies zircons: the age of Alpine metamorphism in the Sesia–Lanzo Zone (Western Alps). Earth Planet. Sci. Lett. 167, 141–158.

Rubatto, D., Hermann, J., Berger, A., Engi, M., 2009. Protracted fluid-induced melting during Barrovian metamorphism in the Central Alps. Contrib. Mineral. Petrol. 158, 703–722.

Rubatto, D., Chakraborty, S., Dasgupta, S., 2013. Timescales of crustal melting in the Higher Himalayan Crystallines (Sikkim, Eastern Himalaya) inferred from trace element-constrained monazite and zircon chronology. Contrib. Mineral. Petrol. 165, 349–372.

Sambridge, M.S., Compston, W., 1994. Mixture modeling of multi-component data sets with application to ion-probe zircon ages. Earth Planet. Sci. Lett. 128, 373–390.

Santamaría, F., Schubert, C., 1974. Geochemistry and geochronology of the southern Caribbean–northern Venezeula plate boundary. Geol. Soc. Am. Bull. 85, 1085–1098.

Schaltegger, U., Fanning, C.M., Günther, D., Maurin, J.C., Schulmann, K., Gebauer, D., 1999. Growth, annealing and recrystallization of zircon and preservation of monazite in high-grade metamorphism: conventional and in-situ U–Pb isotope, cathodoluminescence and microchemical evidence. Contrib. Mineral. Petrol. 134, 186–201.

Sisson, V.B., Ertan, I.E., Avé Lallemant, H.G., 1997. High-pressure (~2000 MPa) kyanite- and glaucophane-bearing pelitic schist and eclogite from Cordillera de la Costa belt, Venezuela. J. Petrol. 38, 65–83.

Sisson, V.B., Avé Lallemant, H.G., Ostos, M., Blythe, A.E., Snee, L.W., Copeland, P., Wright, J.E., Donelick, R.A., Guth, L.R., 2005. Overview of radiometric ages in three allochthonous belts of northern Venezuela: old ones, new ones, and their impact on regional geology. In: Avé Lallemant, H.G., Sisson, V.B. (Eds.), Caribbean–South American Plate InteractionsGeological society of America special papers 394. Geological Society of America, Boulder, pp. 91–117.

Skora, S., Baumgartner, L.P., Mahlen, N.J., Johnson, C.M., Pilet, S., Hellebrand, E., 2006. Diffusion-limited REE uptake by eclogite garnets and its consequences for Lu–Hf and Sm–Nd geochronology. Contrib. Mineral. Petrol. 152, 703–720.

Sláma, J., Košler, J., Condon, D.J., Crowley, J.L., Gerdes, A., Hanchar, J.M., Horstwood, M.S.A., Morris, G.A., Nasdala, L., Norberg, N., Schaltegger, U., Schoene, B., Tubrett, M.N., Whitehouse, M.J., 2008. Plešovice zircon — a new natural reference material for U–Pb and Hf isotopic microanalysis. Chem. Geol. 249, 1–35.

Smith, C.A., Sisson, V.B., Avé Lallemant, H.G., Copeland, P., 1999. Two contrasting pressure-temperature-time paths in the Villa de Cura blueschist belt, Venezuela: possible evidence for Late Cretaceous initiation of subduction in the Caribbean. Geol. Soc. Am. Bull. 111, 831–848.

Smye, M., Stockli, T.M., 2014. Rutile U–Pb depth profiling: a continuous record of lithospheric thermal evolution. Earth Planet. Sci. Lett. 408, 171–182.

Sorensen, S.S., Sisson, V.B., Avé Lallemant, H.G., 2005. Geochemical evidence for possible trench provenance and fluid-rock histories, Cordillera de la Costa eclogite belt, Venezuela. In: Avé Lallemant, H.G., Sisson, V.B. (Eds.), Caribbean–South American Plate InteractionsGeological society of America special papers 394. Geological Society of America, Boulder, pp. 173–192.

Spear, F.S., 2014. The duration of near-peak metamorphism from diffusion modeling of garnet zoning. J. Metamorph. Geol. 32, 903–914.

Spear, F.S., Ashley, K.T., Webb, L.E., Thomas, J.B., 2012. Ti diffusion in quartz inclusions: implications for metamorphic time scales. Contrib. Mineral. Petrol. 164, 977–986.

Speed, R.C., Sharp, W.D., Foland, K.A., 1997. Late Paleozoic granitoid gneisses of Northeastern Venezuela and the North America–Gondwana collision zone. J. Geol. 105, 457–470.

Spencer, K.J., Hacker, B.R., Kylander-Clark, A.R.C., Andersen, T.B., Cottle, J.M., Stearns, M.A., Poletti, J.E., Seward, G.G.E., 2013. Campaign-style titanite U–Pb dating by laser-ablation ICP: implications for crustal flow, phase transformations and titanite closure. Chem. Geol. 341, 84–101.

Stacey, J.S., Kramers, J.D., 1975. Approximation of terrestrial lead isotope evolution by a two-stage model. Earth Planet. Sci. Lett. 26, 207–221.

Stearns, M.A., Cottle, J.M., Kylander-Clark, A.R., Hacker, B.R., 2015. Evaluating lattice diffusion in titanite using coupled U–Pb and trace element depth profiles by single shot-split stream laser ablation (SS-LASS) ICP-MS. Chem. Geol. (in review).

Steely, A.N., Hourigan, J.K., Juel, E., 2014. Discrete multi-pulse laser ablation depth profiling with a single-collector ICPMS: sub-micron U–Pb geochronology of zircon and the effect of radiation damage on depth-dependent fractionation. Chem. Geol. 372, 92–108.

Steiger, R.H., Jäger, E., 1977. Subcommission on geochronology: convention on the use of decay constants in geo- and cosmochronology. Earth Planet. Sci. Lett. 36, 359–362.

Stephan, J.F., 1985. Andes et chaîne Caraibe sur la transversale de Barquisimeto (Venezuela): Evolution géodynamique. In: Alain, M. (Ed.), Symposium Géodynamique des Caraibes, Paris, 5–8 Février 1985, pp. 505–529.

Stöckhert, B., Maresch, W.V., Brix, M., Kaiser, C., Toetz, A., Kluge, R., Krückhans-Lueder, G., 1995. Crustal history of Margarita Island (Venezuela) in detail: constraint on the Caribbean plate tectonic scenario. Geology 23, 787–790.

Trail, D., Mojzsis, S.J., Harrison, T.M., 2007. Thermal events documented in Hadean zircons by ion microprobe depth profiles. Geochim. Cosmochim. Acta 71, 4044–4065.

Urbani, F., Rodrigues, J.A., Omaña, A.L., Tardáguila, P., 2002. "Cartografia Geologica Cordillera de la Costa" a escala 1:25,000: hojas 6647-I-SO, La Candelaria; 6647-II-NO, Cata; 6647-III-NE, Ocumare de la Costa; 6647-III-NO, Borburata. FUNVISIS, Universidad Central de Venezuela, Caracas.

Vance, D., O'Nions, R.K., 1990. Isotopic chronometry of zoned garnets: growth kinetics and metamorphic histories. Earth Planet. Sci. Lett. 97, 227–240.

Vance, D., O'Nions, R.K., 1993. Prograde and retrograde histories from the central Swiss Alps. Earth Planet. Sci. Lett. 114, 113–129.

Viete, D.R., Forster, M.A., Lister, G.S., 2011a. The nature and origin of the Barrovian metamorphism, Scotland: ^{40}Ar/^{39}Ar apparent age patterns and the duration of metamorphism in the biotite zone. J. Geol. Soc. 168, 133–146.

Viete, D.R., Hermann, J., Lister, G.S., Stenhouse, I.R., 2011b. The nature and origin of the Barrovian metamorphism, Scotland: diffusion length scales in garnet and inferred thermal time scales. J. Geol. Soc. 168, 115–132.

Vorhies, S.H., Ague, J.J., Schmitt, A.K., 2013. Zircon growth and recrystallization during progressive metamorphism, Barrovian zones, Scotland. Am. Mineral. 98, 219–230.

Watson, E.B., Liang, Y., 1995. A simple model for sector zoning in slowly grown crystals: implications for growth rate and lattice diffusion, with emphasis on accessory minerals in crustal rocks. Am. Mineral. 80, 1179–1187.

Weber, M., Cardona, A., Valencia, V., Altenberger, U., López-Martinez, M., Tobón, M., Zapata, S., Zapata, G., Concha, A.E., 2011. Geochemistry and geochronology of the Guajira eclogites, northern Colombia: evidence of a metamorphosed primitive Cretaceous Caribbean island-arc. Geol. Acta 9, 425–443.

Wendt, I., Carl, C., 1991. The statistical distribution of the mean squared weighted deviation. Chem. Geol. 86, 275–285.

Wiedenbeck, M., Allé, P., Corfu, F., Griffin, W.L., Meier, M., Oberli, F., von Quadt, A., Roddick, J.C., Spiegel, W., 1995. Three natural zircon standards for U–Th–Pb, Lu–Hf, trace element and REE analyses. Geostand. Geoanal. Res. 1, 1–23.

Wiedenbeck, M., Hanchar, J.W., Peck, W.H., Sylvester, P., Valley, J., Whitehouse, M., Kronz, A., Morishita, Y., Nasdala, L., Fiebig, J., Franchi, I., Girard, J.-P., Greenwood, R.C., Hinton, R., Kita, J., Mason, P.R.D., Norman, M., Ogasawara, M., Piccoli, P.M., Rhede, D., Satoh, H., Schulz-Dobrick, B., Skår, Ø., Spicuzza, M.J., Terada, K., Tindle, A., Togashi, S., Vennemann, T., Xie, Q., Zheng, Y.-F., 2004. Further characterization of the 91500 zircon crystal. Geostand. Geoanal. Res. 28, 9–39.

Woodhead, J., Hergt, J., Shelley, M., Eggins, S., Kemp, R., 2004. Zircon Hf-isotope analysis with an excimer laser, depth profiling, ablation of complex geometries, and concamitant age estimation. Chem. Geol. 209, 121–135.

Ysaccis, R., 1997. Tertiary evolution of the Northeastern Venezuela offshore (PhD Thesis) Rice University, Houston.

Yuan, H.-L., Gao, S., Dai, M.-N., Zong, C.-L., Günther, D., Fontaine, G.H., Liu, X.-M., Diwu, C.R., 2008. Simultaneous determinations of U–Pb age, Hf isotopes and trace element compositions of zircon by excimer laser-ablation quadrupole and multiple-collector ICP-MS. Chem. Geol. 247, 100–118.